Super star clusters in Haro 11: properties of a very young starburst and evidence for a near-infrared flux excess

A. Adamo,[1]⋆ G. Östlin,[1] E. Zackrisson,[1] M. Hayes,[2] R. J. Cumming[1] and G. Micheva[1]

[1]*Department of Astronomy, Stockholm University, Oscar Klein Centre, AlbaNova, Stockholm SE-106 91, Sweden*
[2]*Observatoire Astronomique de l'Université de Genève, 51, ch des Maillettes, CH-1290 Sauverny, Switzerland*

ABSTRACT

We have used multiband imaging to investigate the nature of an extreme starburst environment in the nearby Lyman break galaxy analogue Haro 11 (ESO 350−IG038) by means of its stellar cluster population. The central starburst region has been observed in eight different high-resolution *Hubble Space Telescope* (*HST*) wavebands, sampling the stellar and gas components from UV to near-infrared. Photometric imaging of the galaxy was also carried out at 2.16 μm by NaCo AO instrument at the ESO Very Large Telescope. We constructed integrated spectral energy distributions (SEDs) for about 200 star clusters located in the active star-forming regions and compared them with single stellar population models (suitable for physical properties of very young cluster population) in order to derive ages, masses and extinctions of the star clusters. The cluster age distribution we recover confirms that the present starburst has lasted for 40 Myr, and shows a peak of cluster formation only 3.5 Myr old. With such an extremely young cluster population, Haro 11 represents a unique opportunity to investigate the youngest phase of the cluster formation process and evolution in starburst systems. We looked for possible relations between cluster ages, extinctions and masses. Extinction tends to diminish as a function of the cluster age, but the spread is large and reaches the highest dispersion for clusters in partial embedded phases (<5 Myr). A fraction of low-mass (below $10^4 M_\odot$), very young (1–3 Myr) clusters is missing, either because they are embedded in the parental molecular cloud and heavily extinguished, or because of blending with neighbouring clusters. The range of the cluster masses is wide; we observe that more than 30 per cent of the clusters have masses above $10^5 M_\odot$, qualifying them as super star clusters. Almost half of the cluster sample is affected by flux excesses at wavelengths >8000 Å which cannot be explained by simple stellar evolutionary models. Fitting SED models over all wavebands leads to systematic overestimates of cluster ages and incorrect masses for the stellar population supplying the light in these clusters. We show that the red excess affects also the *HST F*814*W* filter, which is typically used to constrain cluster physical properties. The clusters which show the red excess are younger than 40 Myr; we discuss possible physical explanations for the phenomenon. Finally, we estimate that Haro 11 has produced bound clusters at a rate almost a factor of 10 higher than the massive and regular spirals, like the Milky Way. The present cluster formation efficiency is ∼38 per cent of the galactic star formation rate.

Key words: galaxies: irregular – galaxies: starburst – galaxies: star clusters: individual: Haro 11.

1 INTRODUCTION

Young star clusters (SCs) are luminous and quite compact objects which in some ways resemble older massive globular clusters. However, while these old systems are 'passively' fading due to stellar and secular evolution, young SCs are still, or in most of the cases, embedded in their dusty cocoons and at constant risk of destruction by interactions with the interstellar medium, internal feedback, tidal forces and evaporation (see Larsen 2009b, and references therein). The youngest phases, when the cluster is still partially embedded in its natal molecular cloud, are difficult to explore because of the high extinction levels which introduce uncertainties in age and mass estimates. Lada & Lada (2003) observed that the embedded phase

⋆E-mail: adamo@astro.su.se

in young Milky Way (MW) clusters lasts a few million years. Very young clusters in the Antennae (Whitmore & Zhang 2002) system, with ages ≤4 Myr, show a wide range of extinction within $0.5 \leq A_{\rm V} \leq 7.6$ mag. Whitmore & Zhang 2002 identified an additional population of 'red clusters', which they interpreted as young embedded clusters. Among them, the 2-Myr-old WS 80, with its extreme $V - I = 2.92$ colour, mass 4×10^6 M$_\odot$ and $A_{\rm V} = 7.6$ mag, is the brightest infrared (IR) source in the Antennae system. Whitmore & Zhang (2002) indicated roughly 6 Myr as the age at which a young cluster has gotten rid of the dusty material left over from its parent cloud. In another galaxy, NGC 4449, Reines, Johnson & Goss (2008a) found 3–5 Myr old clusters with relatively low extinctions ($A_{\rm V} \leq 1.5$ mag). Although these very early stages are fundamental for our understanding of cluster formation, evolution and possible destruction (90 per cent of clusters are not expected to survive after their first 10 Myr; Lada & Lada 2003), they are still poorly understood.

The cluster formation process is intimately connected both to the galactic environment via the star formation efficiency (SFE), and on long time-scales, to the global star formation history (SFH) of the galaxy. Interactions and/or merging between gas-rich galaxies provide physical conditions which favour the formation of SCs and enhance star formation rates (SFRs). SCs are easily detected in active star-forming regions inside normal spiral galaxies (Larsen 2002; Cantiello, Brocato & Blakeslee 2009); in starburst galaxies, like M 82 (Konstantopoulos et al. 2009, and references therein) and NGC 3310 (de Grijs et al. 2003a,b); interacting (Bastian et al. 2005) and merging systems (Whitmore et al. 1999; Wilson et al. 2006; Väisänen et al. 2008) to cite only a few examples. Interestingly, very bright and massive clusters have also been detected in smaller and less regular systems, like the dwarf post-starburst galaxies NGC 1569 (Anders et al. 2004b) and NGC 1709 (Billett, Hunter & Elmegreen 2002; Annibali et al. 2009) and in blue compact galaxies (BCGs), which are active dwarf starburst galaxies with low metallicity (Östlin et al. 2003; Adamo et al. 2009; Adamo et al., in preparation).

The cluster initial mass function (CIMF) and the cluster luminosity function (CLF) are directly connected to the star formation processes which act from stellar to galactic scales, due to the clustered nature of star formation (Lada & Lada 2003). In general, the CIMF can be approximated by a power-law relation of the type $\mathrm{d}N(M)/\mathrm{d}M = CM^{-\gamma}$, where $\gamma \approx 2$ (Zhang & Fall 1999; Bik et al. 2003; Hunter et al. 2003). The CLF, $\mathrm{d}N(L) \propto L^{-\alpha}\mathrm{d}L$, on the other hand, has been shown to have wider range of the index values, $1.8 \leq \alpha \leq 2.7$, and in some cases is better fitted with a double power law with a break in the range $-10.4 \leq M_{\rm V} \leq -8$ mag (Whitmore et al. 1999; Larsen 2002; Gieles et al. 2006b). In a galaxy, the CLF is the synthesis of several populations of SCs assembled at different ages. For this reason, the CLF contains imprints of both the mechanisms behind cluster evolution and the initial environmental conditions where the clusters form. A number of studies have shown that high star formation levels enable a better sampling of the LF up to its brighter end and in turn determine the formation of the brightest cluster in a galaxy (Larsen 2002; Gieles et al. 2006a,b; Bastian 2008; Gieles 2009; Larsen 2009a). On the other hand, physical factors also put constraints on the mass (and consequently the luminosity) of the clusters which are born, such as mass of the parent giant molecular cloud (GMC) and the pressure and density of the interstellar medium (Billett et al. 2002; Hunter et al. 2003; Lada & Lada 2003). Gieles et al. (2006a) noted that if physical conditions in the galactic environment limit the maximum value of the cluster mass, leading to a truncated CIMF, this effect

will appear in the LF as a break which corresponds to the maximum cluster mass at the oldest age the galaxy can form.

In this paper we focus our attention on the BCG Haro 11 (ESO 350−IG038), which has been shown to be extremely efficient in producing SCs. Generally, BCGs have magnitude between $M_B \approx -12$ and $M_B \approx -21$ (Kunth & Östlin 2000). They are characterized by an ongoing active starburst phase with high SFRs, producing their typical high surface brightness and prominent nebular emission-line spectra. Photometric studies of their galactic stellar populations have revealed the presence of an old underlining stellar component (Kunth, Maurogordato & Vigroux 1988; Bergvall & Östlin 2002; Micheva et al. 2010). Thanks to the resolution power of the *Hubble Space Telescope* (*HST*), it has been possible to resolve the BCG burst regions into many bright SCs implying that the star formation is remarkably efficient. However, it still not clear yet how systems with masses $\leq 10^{10}$ M$_\odot$ can form such large numbers of SCs. Billett et al. (2002), investigating a sample of 22 nearby (<7 Mpc) dwarf starburst and post-starburst galaxies, noted that dwarf starburst galaxies have luminosities brighter than $M_{\rm V} = -16$ and pointed out that despite their sizes, they are able to host very massive clusters. Whether this is a consequence of stochastic sampling effects of the CIMF in combination with environmental conditions which favour the formation of SCs with $M \geq 10^5$ M$_\odot$ or different cluster formation physics is not yet established. In this paper, we will call clusters with masses $\geq 10^5$ M$_\odot$ super star clusters (SSCs).

In Fig. 1, we show a three-colour image of Haro 11. The three main starburst regions, called knots A, B and C by Kunth et al. (2003), are easily traced in the heart shape. Dust filaments cross knot B and are present in all the burst regions. Haro 11 is a Lyα and Lyman continuum emitter (Hayes et al. 2007) and can be considered a local analogue (Overzier et al. 2008) of the high-redshift Lyman break galaxies (LBGs). Moreover, Haro 11's IR luminosity of 1.9×10^{11} L$_\odot$ (Section 6.2) locates Haro 11 in the range of the luminous IR galaxies (LIRGs). Östlin et al. (2001), studying the Hα velocity field, found that the mass estimate from rotation curves is lower than the photometric one, probably because the galaxy is not rotationally supported, perhaps because the gas is not in dynamical equilibrium. The total estimated stellar mass is $\approx 10^{10}$ M$_\odot$. Haro 11's perturbed morphology, multiple-component Hα velocity field and high SFR are all signatures of a merger between a low-mass, evolved system and a gas-rich component. Interestingly, Östlin et al. (2001) have estimated that the present burst in Haro 11 has been active for ∼35 Myr, and using the mass of neutral hydrogen, H I estimated by Bergvall et al. (2000), a gas consumption time-scale (i.e. remaining lifetime) of ∼5 Myr for the present burst phase. We estimated in Section 6.2 that the present SFR in Haro 11 is of 22 ± 3 M$_\odot$ yr^{-1}. If we take into account the total mass of gas in H I, H II, H$_2$ and photodissociation regions, then $M_{\rm H}^{\rm tot} \sim 2 \times 10^9$ M$_\odot$ (Bergvall et al. 2000) and we find that the present burst would last at least 100 Myr at its current rate. These time-scales show that the gas consumption in the galaxy is currently very rapid but its future development is highly uncertain.

Finally, the similarity between this galaxy and the high-redshift LBGs provides an opportunity to constrain the star-forming mechanisms of the earliest galaxies, when the metallicity was low and the environments were unrelaxed and chaotic.

This paper, together with the analysis done by Östlin et al. (2003) and two future publications on the BCGs ESO 185−IG03 and Mrk 930, will be part of a statistical analysis to constrain and define the major properties of the SSC populations in BCGs.

The paper is organized as follows. In Sections 2 and 3 we describe in detail our data reduction and cluster detection method. Section 4
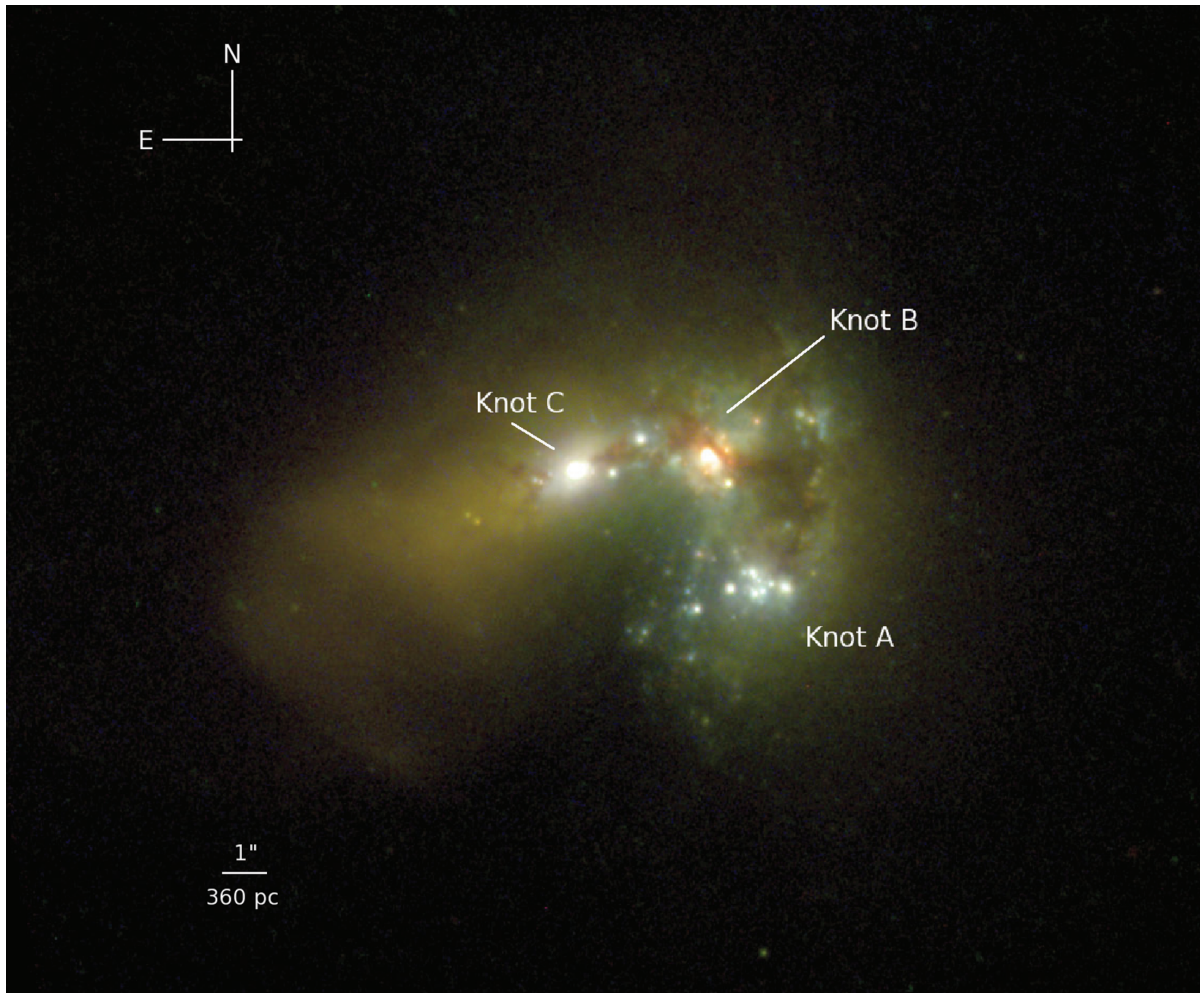
Figure 1. The starburst regions in Haro 11. The image is the result of the combination of the WFPC2 *F*814*W* filter in red, and the two ACS filters: *F*435*W* in green and *F*220*W* in blue. The orientation and the 1 arcsec length are indicated. The names of the three starburst regions are the same as in Kunth et al. (2003).

focuses on the estimation of the clusters' physical properties, in particular ages, masses and extinction. In this section we also assess the evidence for flux excesses at red wavelengths. Section 5 we examine the possible causes of the red excess. In Section 6 we report on the properties of the host galaxy as showed by the cluster analysis. In Section 7 we collect our main conclusions.

The luminosity distance and distance modulus of Haro 11 are estimated to be 82.3 Mpc and $(m - M) = 34.58$ mag,[1] respectively, assuming a cosmology of $H_0 = 73 \, \text{km s}^{-1} \, \text{Mpc}^{-1}$, $\Omega_M = 0.27$ and $\Omega_\Lambda = 0.73$ throughout.

2 DATA SAMPLE AND REDUCTIONS

A summary of the full data set used in the present analysis[2] is given in Table 1. We have used archival[3] *HST*/ACS imaging of Haro 11, with observations from the *FUV* to the optical

($\sim$8000 Å) wavebands. We have supplemented these data with new[4] *HST*/WFPC2 broad-band imaging in *V* (*F*606*W*), *I* (*F*814*W*) and *H* [NIC3/*F*160*W*; NICMOS near-IR (NIR)]. To sample further into the IR we have used the NaCo adaptive optics (AO) imager in the K_s band.[5] Unless otherwise specified, we use the Vega magnitude system throughout the paper. The zero-points (ZPs) in Vega magnitudes are given in Table 1 for all the filters.

2.1 ACS data reduction

A full description of the data reduction of the archival data is given in Östlin et al. (2009). The final ACS images have all been drizzled and aligned using the MULTIDRIZZLE task (Fruchter & Hook 2002; Koekemoer et al. 2002) in PYRAF/STSDAS[6] and rescaled to the HRC pixel scale, that is 0.025 arcsec px^{-1}. The final science images are rotated to north up. The short HRC *F*814*W* exposure was only used for estimating the flux of the two brightest sources, in the centre of

---

[1] Value taken from NASA/IPAC Extragalactic Database (NED).

[2] Based on observations made with the NASA/ESA *HST*, obtained at the Space Telescope Science Institute, which is operated by the Association of Universities for Research in Astronomy, Inc., under NASA contract NAS 5-26555.

[3] Associated with programmes # GO 9470 (PI D. Kunth) and # GO 10575 (PI G. Östlin).

[4] Associated with programmes # GO 10902, PI G. Östlin.

[5] Based on observations made with ESO telescopes at the Paranal Observatory under programme IDs 079.B-0585 and 081.B-0234. The observations were carried out the 2008 July 24.

[6] STSDAS and PyRAF are products of the Space Telescope Science Institute, which is operated by AURA for NASA.

Table 1. Haro 11: *HST* observations. Archival observations are associated with programmes # GO 9470 (PI D. Kunth) and # GO 10575 (PI G. Östlin). The new observations were obtained in the programme # GO 10902 (PI G. Östlin). The ZP in Vega magnitude system, and the aperture correction, a_c, to the point-source photometry are included for each filter. The last two columns show the number of objects detected with a S/N $\geq$ 5, and the corresponding magnitude limit in each frame.

Filter	Instrument	Exposure time (s)	ZP (mag)	a_c (mag)	$N(\sigma \leq 0.2)$	Magnitude limit
	Archival observations					
F140LP (FUV)	ACS/SBC	2700	20.92	-0.49 ± 0.05	113	25.1
F220W (NUV)	ACS/HRC	1513	21.88	-0.41 ± 0.05	80	23.2
F330W (U)	ACS/HRC	800	22.91	-0.35 ± 0.05	90	23.7
F435W (B)	ACS/WFC	680	25.79	-0.50 ± 0.05	178	27.5
F550M (V)	ACS/WFC	471	24.88	-0.45 ± 0.05	144	26.2
F814W (I)	ACS/HRC	100	24.86	-0.56 ± 0.07	$-^a$	$-^a$
	New observations					
F606W (R)	WFPC2/PC	4000	22.89	-0.61 ± 0.09	211	27.5
F814W (I)	WFPC2/PC	5000	21.64	-0.73 ± 0.04	211	26.2
F160W (H)	NIC 3	5000	21.88	-2.45 ± 0.37	71	25.6
K_s	VLT/NaCo	1222	23.32	-2.15 ± 0.64	66	20.5

^{a}Shallower image used only to do photometry in the two central cluster regions saturated in the deeper exposure.

knots *B* and *C* (Fig. 1). Both knot centres were saturated in the deep WFPC2 *F*606*W* and *F*814*W* exposures.

2.2 WFPC2 data reduction

Due to the small size (major axes ∼13.0 arcsec) of the starburst regions into the galaxy, the target could easily fit into the high-resolution (pixel scale is 0.045 arcsec) planetary camera (PC) which has a field of view (FOV) of 35 × 35 arcsec². In order to refine the WFPC2 resolution we used subpixel dithering and combining patterns. The data reduction was performed with MULTIDRIZZLE. We took into account sky corrections during the photometric analysis rather than performing sky subtraction with MULTIDRIZZLE. Before combining the final image, we resized the pixel scale to 0.025 arcsec, applying a drop size of 0.8 for both the filters, and rotated the final image so that north was up.

2.2.1 The WFPC2 point spread function

Because we found no isolated bright objects either in the galaxy or in the PC field, we constructed a filter-dependent point spread function (PSF) using archival data. We retrieved WFPC2/*F*814*W* images of the NGC-104-F field of the globular cluster 47 Tuc (# GO 8160, PI I. King). This field was chosen because it is not crowded and has dithering path and exposure time comparable to our data. We built the *F*606*W* PSF in a similar fashion using data from another uncrowded stellar field (# GO 8090, PI S. Casertano). We reduced the images applying the same method, taking into account only the PC field of the mosaic. Isolated sources in the field were selected by eye, and encircled energy distributions for each of them were inspected in order to avoid sources with irregular PSF shapes. The tasks PSTSELECT and PSF were used to produce the final PSF. These two constructed PSFs were used to perform a completeness test (see Section 3.2).

2.3 NICMOS data reduction

The NIC3 camera was chosen because of the size of the FOV, 51.2 × 51.2 arcsec². To subsample and improve the pixel scale resolution (for NIC3, the plate scale is ∼0.2 arcsec px^{-1}) a double

NIC-SPIRAL-DITH path with three dithered pointings each was applied in order. The single science frames showed significant differences in the sky background levels and presence of bias residuals, which we corrected before running MULTIDRIZZLE. In order to get the best combination of pixel subsampling and pixel drop size values we compared the flux growth curves of some bright point-like objects in the final science frame with a reference model PSF produced by TINYTIM software.[7] The resulting best set of input values for the final combined image was found to be pixscale = 0.067 arcsec px^{-1} and pixfrac = 0.7. The pixel scale applied to the final frame is the diffraction limited value for the NIC3 camera. The final science frame was rotated to north up and calibrated in units of *DN/s*. We performed a number of tests of the calibration of the final IR frame: these are detailed in Appendix A.

2.4 NaCo data reduction

K_s imaging was carried out at the Very Large Telescope (VLT) UT4 telescope using Naos–Conica (NaCo) AO instrument in natural guide star mode. The CONICA imager and spectrograph equipped with the Aladdin3 array and S27 camera (FOV of 28 × 28 arcsec²) was chosen. The chopping mode and dithering path were set and a total of 24 target images and 24 sky fields were taken, each with DIT = 9.4 s averaged on 13 NDITs. We used PYPELINE (Micheva et al. 2010) for bad-pixel masking, pair subtraction, flat-field correction, source masking, sky background subtraction and alignment. Before the final stacking, the quality of every frame was checked and those with blurred PSFs were excluded, in order to achieve the best possible resolution. Frames with PSF full width at half-maximum > 4 px (∼0.108 arcsec) were rejected. The final image was built from the median of the best 10 selected frames (corresponding to a total exposure time of 1222 s). A standard star was observed the same night, with the same instrumental set, and at comparable airmass values that for our target (the difference is <0.08) so that the ZP value is affected by the same atmospheric extinction value as the galaxy. The pixel scale in the final frame was 0.027 arcsec px^{-1}.

[7] http://www.stsci.edu/software/tinytim/

# 3 CLUSTER SELECTION AND PHOTOMETRY

3.1 Cluster detection

SEXTRACTOR (Bertin & Arnouts 1996) was used to find sources in the deep *R* and *I* WFPC2 exposures. The starburst in the galaxy is intense and many point-like sources lie in crowded regions and superimposed on the bright galactic background. Farther out of the main body, point-like sources can be still observed but now in empty regions with lower background values. In order to extract candidate clusters in all these different regions of the galaxy field we ran SEXTRACTOR twice on each frame, each time with different input parameters. To find sources in the outskirts of the galaxy, we used a detection threshold of 2σ above the background rms noise, a minimum of four adjacent pixels and a minimum contrast for deblending set to the default value, 0.001. To detect sources into the starburst region we increased the detection threshold to 2.5σ, applied one of the mexhat filters available in SEXTRACTOR and raised the value of the deblending minimum contrast to 0.005. In this way we avoided large numbers of spurious detections while at the same time being able to separate blended sources in crowded regions. The two lists of coordinates were then merged into a unique catalogue, cleaned from multiple detections of the same object and from sources separated by less than the diffraction limit of the telescope. We fixed a centre for the galaxy ($\alpha = 00 : 36 : 52 : 62.7$, $\delta = -33\,33\,17.49$) and delimited detections to a region of radius of 13.75 arcsec around the centre. Finally, detections in the two cleaned *R*- and *I*-band catalogues were cross-checked. All the sources which were not detected in both *R* and *I* catalogues were discarded. The final catalogue comprised 563 objects.

For the two WFPC2 images, we performed a correction for charge transfer efficiency effects on the observed fluxes using the algorithm of Dolphin (2009). Because of the complexity of the region, i.e. point-like sources located in the extended luminous background of the galaxy, we chose not to use the median background value, as prescribed by Dolphin's formula. Instead we estimated a 'local' background for each source, given by the median value of the pixel columns above the source, where few a per cent of the total charge has probably been trapped.

We show the 563 cluster candidates in the colour–magnitude diagram in Fig. 2.

3.2 Completeness limits

To test the method we used to constrain the source catalogue and the detection limits, we performed a completeness analysis for both *R* and *I* WFPC2 frames. A mock catalogue was made with objects positioned along a grid of 30 pixels per side (big enough not to increase crowding). All the positions were located inside the circle defined previously. Magnitudes were randomly assigned to each position, from 19.0 to 29.0 mag with an interval of 0.5. For each filter, we created a synthetic frame with the sources using MKSYNTH, a task of the publicly-available software toolkit BAOLAB (Larsen 1999). We supplied the PSF shape. The object detection was done in the same way as previously explained and no conditions were placed on the photometry. We then counted how many of the input objects were recovered, allowing a displacement not larger than 1.5 pixels. We repeated the procedure three times, shifting the grid by 10×10 pixels and re-assigning magnitude randomly to prevent introduction of systematics. The mean recovered fractions of objects as a function of magnitude is shown in Fig. 3. The completeness goes down to
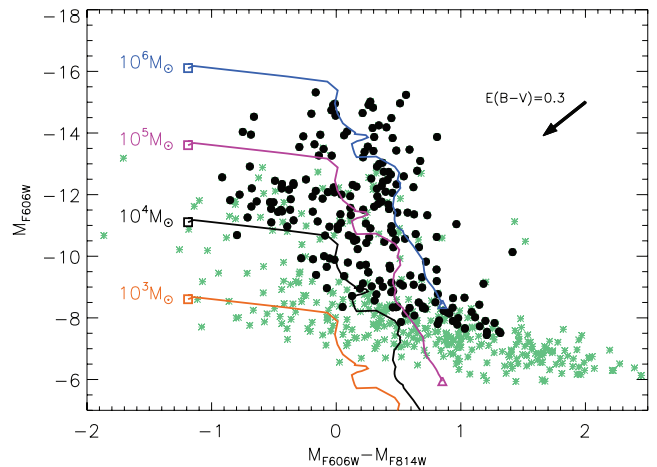
Figure 2. Colour–magnitude diagram for the 563 cluster candidates detected in both *R* and *I* filters. The black filled dots are the 211 sources with a signal-to-noise ratio (S/N) ≥ 5 in both filters (see Table 1). Model evolutionary tracks with metallicity $Z = 0.004$ are from Z01. The masses corresponding to each track are indicated. The thick squares show the model starting point at 1 Myr, the triangles show the end point at 14 Gyr. The arrow shows the direction of a correction for extinction of $E(B - V) = 0.3$. Colour versions of all figures are available in the online journal.
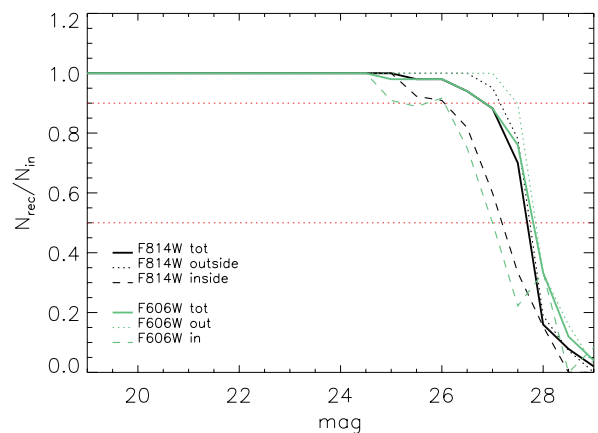
Figure 3. Recovered fractions of sources as a function of their magnitude for *R* and *I* images. The two continuous thick lines are the completeness limits for detection in filters *F814W* (black) and *F606W* (green). The dotted (dashed) line shows the recovered fractions inside (outside) the crowded starburst region, as defined in Section 3.1. The two red dotted horizontal lines show the 90 and 50 per cent completeness levels.

90 per cent at magnitude 27 in both filters, and only 50 per cent of objects are recovered at ~ 28.0 mag.

This is an averaged result: in reality, incompleteness due to crowding in the central active star-forming region is larger than that in the outskirts of the galaxy. To assess by how much, we did a second completeness estimation, this time distinguishing between the two regions, with boundary radius fixed at 6.5 arcsec from the centre. The fraction of recovered objects inside the crowded region (dashed and dotted lines in Fig. 3) begins to diminish in both *R* and *I* frames at between 25.0 and 25.5 mag, reaching 90 per cent already at ~ 26.0 mag and dropping to 70 per cent at 27.0 mag. On the other hand, the recovered fraction of objects outside the crowded region gives 100 per cent completeness for detections as faint as 27.0 mag. As expected, blending affects the detections at the faint end of the CLF in the active starbursting region.

3.3 Photometry and final catalogue

Aperture photometry was performed with the task PHOT, in all the available filters, using the catalogue previously determined. The IRAF tasks GEOMAP and GEOXYTRAN were used to transform the coordinates from the WFPC2 system to the corresponding ACS, NICMOS and NaCo/S27 catalogues. Growth curves of several objects in different filters were investigated to decide the size of the aperture radius. Finally, we carried out photometry in all frames using a fixed aperture radius of $a_r = 0.1$ arcsec and estimating the local sky background in an annulus of internal radius $s_r = 0.125$ arcsec and width 0.05 arcsec. In order to avoid photometric uncertainties affecting the age and extinction estimates, we rejected for each filter data points with magnitude errors $\sigma_m > 0.2$. In Table 1 we show the corresponding magnitude limits and the number of objects in each frame after this selection. For the final catalogue, we retained only objects detected in at least three filters. In total it contains 198 objects.[8] Galactic extinction corrections in all the filters were applied. Only 17 per cent (34/198) of sources had detection in three filters, 21 per cent in four, 12 per cent in five, 11 per cent in six, 13 per cent in seven, 12 per cent in eight and 14 per cent (28/198) in the nine available filters. In total, 83 per cent of the objects in the catalogue had detections in at least four filters.

Aperture corrections and associated errors were estimated for each filter frame and added to the fluxes and photometric errors which we previously determined. They are given in Table 1. We used TINYTIM PSF simulator to estimate the aperture corrections values for ACS and WFPC2 frames. A different method was applied to the two IR filter frames, H and K_s. The H frame has a wider PSF and lower pixel scale resolution. For these reasons, we decided to estimate the aperture correction directly from isolated bright star-like objects in the frame. In the large FOV of the NIC3 camera we could identify some point-like objects. Moreover an identical set of NICMOS data was available for other two BCGs, Mrk 930 and ESO 185−13 (part of the same project # GO10902, see Adamo et al. (2009); results will be published in a follow-up paper, Adamo et al., in preparation) and also in those frames, reduced in the same way, few star-like objects were available. The aperture used to do photometry (0.1 arcsec) was quite small and corresponded to half a size of the original NIC3 pixel scale (0.2 arcsec), making the error due to the aperture correction large. On the other hand, using bigger radius apertures would introduce blending of sources. The aperture correction for the K_s image was derived from three bright isolated point-like objects in the frame. In this case the problem was not the poor pixel resolution scale, but the effect of the AO technique on the PSF shape. The flux of the source is split between the diffraction-limited Gaussian PSF core and the extended wings, making the aperture correction PSF dependent. As expected, the aperture correction value is high $a_c = -2.15 \pm 0.64$ because a considerable part of the flux is contained in the PSF wings and the associated error is large.

4 SPECTRAL ENERGY DISTRIBUTION FITTING AND CLUSTER ANALYSIS

4.1 Models

For our spectral energy distribution (SED) fits of the target clusters, we have used the Zackrisson et al. (2001, hereafter Z01) spectral

synthesis model. This model predicts the combined SED of both stars and photoionized gas. Often neglected, the gas component can actually have a pronounced impact on the broad-band fluxes of very young stellar populations (e.g. Krüger, Fritze-v. Alvensleben & Loose 1995; Anders & Fritze-Alvensleben 2003; Zackrisson, Bergvall & Leitet 2008).

The Z01 model, which includes pre-main-sequence evolution and a stochastic treatment of horizontal branch morphologies at low metallicities, is based on synthetic stellar atmospheres by Lejeune, Cuisinier & Buser (1998) and Clegg & Middlemass (1987), together with stellar evolutionary tracks mainly from the Geneva group. The gas continuum and emission lines are predicted using the photoionization code CLOUDY, version 90.05 (Ferland et al. 1998). At each time-step, the SED of the integrated stellar population is fed into CLOUDY, which then provides a realistic evolution of the emission-line ratios over time. The spectra predicted by the models are redshifted to match the target galaxies and convolved with the transmission profiles of the filters used.

In the Z01 model, we assume a stellar metallicity of $Z_{stars} = 0.004$, a Salpeter IMF ($dN/dM \propto M^{-2.35}$) throughout the mass range 0.08–120 $M_\odot$ and an instantaneous burst (i.e. single-age) population. A conversion factor is applied to correct the estimated cluster masses to a Kroupa IMF (Kroupa 2001) in the mass range 0.01–120 $M_\odot$. The properties of the nebular component are determined by the adopted gaseous metallicity Z_{gas}, the hydrogen number density $n(H)$, the gas filling factor f and the gas mass M_{gas} available for star formation. We adopt $n(H) = 100$ cm^{-3} and $f = 0.01$ (values typical for H II regions), a gas metallicity identical to the stellar one ($Z_{gas} = Z_{stars}$) and a gas mass of $M_{gas} = 10^6$ $M_\odot$. Finally, we have used the spectral synthesis model of Marigo et al. (2008, hereafter M08) to test the robustness of some of our conclusions. This model features a more refined treatment of thermally pulsating asymptotic giant branch (AGB) stars (which mainly affects the interpretation of NIR data), but does not include nebular emission. For this reason it is not suitable for the analysis of clusters at ages ≤ 10 Myr (Z01).

### 4.2 Constraining the physical properties of the SCs

4.2.1 χ^2 method

We used a least-squares fit to estimate for each cluster the best fit to our models (similar to other previous works, see Anders et al. 2004a and Bik et al. 2003). Internal extinction was treated as a free parameter, and we used the Calzetti extinction law (Calzetti et al. 2000), allowing extinction varying from $E(B - V) = 0.0$ to 3.0 with a step of 0.01. The Q-value[9] and the reduced $\chi_r^2 = \chi^2/\nu$ were calculated. The $\nu = N - m$ is the number the degrees of freedom. In our case, for each cluster, the number of detections in different filters, $N \geq 3$, while the number of parameters $m = 3$ (the age, mass and extinction of the cluster). The Q-value is a statistical measurement of the goodness of the fit (Press et al. 1992). Q and χ_r^2 were estimated only for clusters with at least detection in four different filters ($N > 3$).

Among our initial model fits, we noted several cases for which $\chi_r^2 \gg 1$ and $Q < 10^{-5}$. For those cases, the inspection of the

---

[8]The complete photometric catalogue is available at http://www.astro.su.se/~adamo or on request from the authors.

[9]Also known as the χ^2 probability function (see Press et al. 1992). Best-fitting models with values of Q, which exceed 0.1, are good representative of the observed data; values of $Q > 0.001$ can be considered still acceptable; while models with lower values are unlikely.
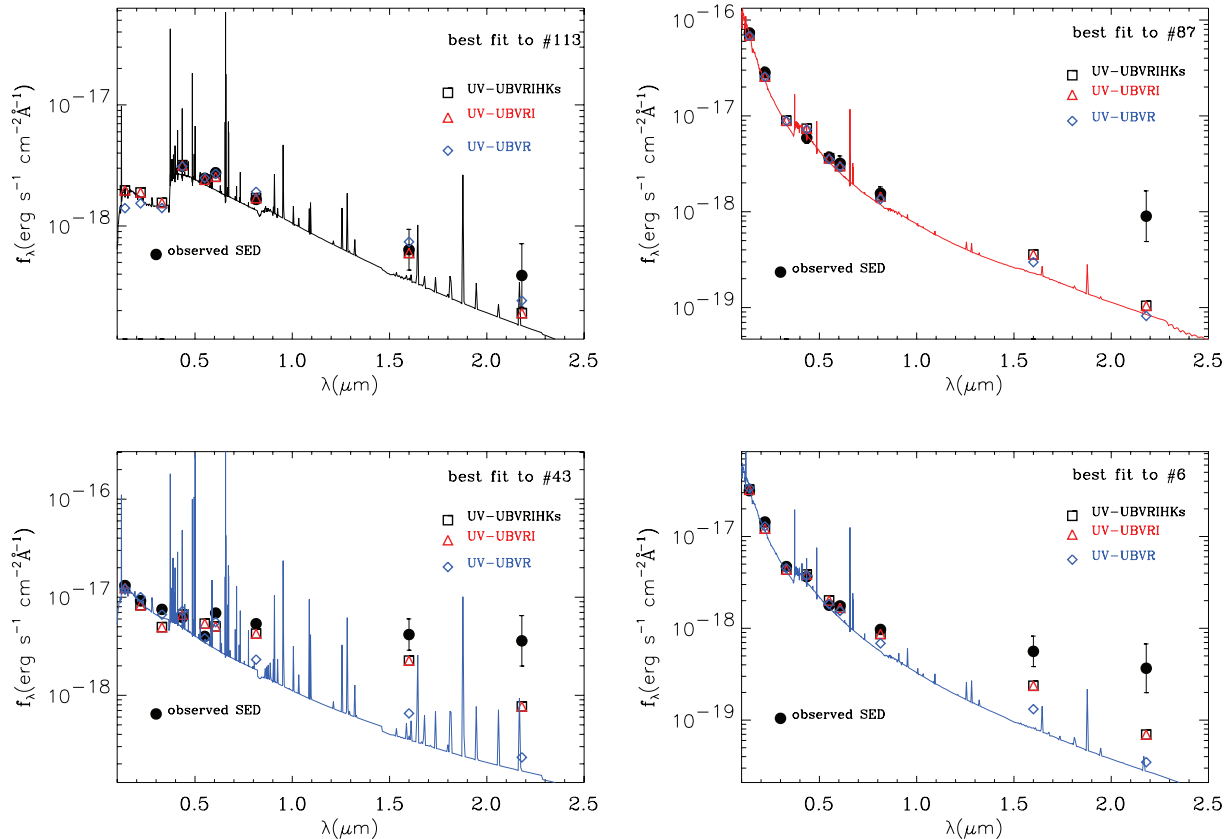
Figure 4. SED analysis of four clusters. The filled black points indicated the observed photometric values of each cluster. The integrated model fluxes are labelled with different symbols for each set of fits as indicated in the plots. We plotted the spectrum of the final best-fitting model with a colour which corresponds to the type of fit.

residuals (displacements between the modelled and the observed integrated photometry of the cluster, $\Delta m = m_{mod} - m_{obs}$), revealed an unusual positive offset, or 'excess', of the observed fluxes in H, K_s and I bands. We performed two further sets of χ^2 fits, this time excluding the NIR data. The first of these we refer to as $UV - UBVR$, where only the six bluer filters were included in the fit. The second set included seven filters, FUV, NUV, U, B, V, R and I, indicated as $UV - UBVRI$. The initial fit, including all the available data from UV to near-IR, we denote $UV - UBVRIHK_s$. We maintained the requirement of at least detections in three filters for each SED fit. This restriction meant that we could fit 190 objects when the H and K_s bands were excluded in the $UV - UBVRI$ fit. Of these, 35 per cent have detections in all the seven included bands, while 22 per cent have detections in only three filters. When the I band was excluded, the number of objects fitted decreased to 149 (23 per cent with at least three detections and 45 per cent with detections in all the allowed filters).

4.2.2 Investigating the excess at near-IR wavelengths

In this section we present 'observational' evidence for the red excess and at the same time probe that the fit to the UV–blue optical integrated fluxes of the clusters produces robust constraints of the cluster properties.

In Fig. 4 we show an example of the three different fits to the integrated SED data points for four different clusters with different physical properties (a table with integrated photometry of these clusters is presented in Appendix B). The quantities plotted

have been converted from Vega magnitudes to physical flux units, erg s^{-1} cm^{-2} Å^{-1}. Integrated photometric data points with associated error bars are plotted together with the best synthetic data points obtained by the three different types of fit: $UV - UBVRIHK_s$ (black squares), $UV - UBVRI$ (red triangles) and $UV - UBVR$ (blue diamonds). The underlying spectrum represents the best model. The

Table 2. Final outputs given by the three sets of SED fits as shown in Fig. 4. In bold we show the final age, mass and extinction assigned to the clusters.

ID	χ_r^2	Q	Myr	$10^5\,M_\odot$	$E(B-V)$
		$UV - UBVRIHK_s$			
113	**0.7**	**0.72**	**5.5**	**1.4**	**0.44**
87	1.65	0.25	10.5	1.3	0.0
43	13.6	$<10^{-5}$	45.0	16.3	0.23
6	3.28	0.006	12.5	0.8	0.0
		$UV - UBVRI$			
113	0.45	0.5	5.5	1.4	0.44
87	**1.1**	**0.34**	**10.5**	**1.3**	**0.0**
43	13.1	$<10^{-5}$	45	16.0	0.23
6	2.6	0.008	12.5	0.8	0.0
		$UV - UBVR$			
113	–	–	5.5	1.8	0.5
87	0.8	0.31	9.5	1.2	0.0
43	**1.4**	**0.07**	**3.5**	**1.5**	**0.34**
6	**1.3**	**0.41**	**8.5**	**0.5**	**0.01**

broad *F*606*W* filter transmits the prominent Hα emission line. So in cases where we see a pronounced jump between fluxes in the narrow *F*550*M* and the broad *F*606*W* filter we expect young (≤8.5 Myr) stellar complexes (e.g. see clusters # 43 and # 113 in Fig. 4). The displacement between these two data points is negligible already around 10 Myr (e.g. cluster # 6 in Fig. 4). Finally, the data points sampling the *U* − *UV* part of the spectrum are extremely sensitive to the internal extinction of the cluster. In Table 2 we list the statistical results and best-fitting parameters obtained with all three sets of fits.

The fit to cluster # 113 is quite good all the way from the UV to the IR (inside the error bars). Looking at Table 2, we see that removing filters from the fit produces no noticeable effect. The jump between *V* and *R* clearly confirms the young age of this object. The non-detection in the UV part of the spectrum is in agreement with the high extinction value. The properties of 83 clusters with similar SED fits to this cluster were estimated by the *UV* − *UBVRIHK*$_s$ fit.

The *UV* − *UBVRIHK*$_s$ fit to the cluster # 87 clearly failed to fit the integrated IR flux in *K*$_s$, sitting above the best-fitting model with an excess of $\Delta m_{K_s} = 2.34$ mag. The large error associated with the observed flux in *K*$_s$ produces a smaller effect on the χ_r^2 and *Q* values of the *UV* − *UBVRIHK*$_s$ fit. Taking into account this factor, even small differences in χ_r^2 and *Q*, as observed here between the *UV* − *UBVRIHK*$_s$ and *UV* − *UBVRI* fits, become important. In this case, we discarded the *UV* − *UBVR* fit solution because, as indicated in Table 2, the exclusion of the *I* band from the fit does not give any improvement. We found 26 clusters with an excess at the IR wavelengths (*H* and *K*$_s$). For these objects, the final ages, masses and extinctions were derived from a *UV* − *UBVRI* fit.

The fits to cluster # 43 give even more dramatic results. Neither the *UV* − *UBVRIHK*$_s$ nor the *UV* − *UBVRI* fits are good (high χ_r^2 and high *Q*). The estimated age, 45 Myr, is impossible to reconcile with the jump observed between the narrow *V* and broad *R* filters, and the estimated mass is high. Excluding the *I*-band photometry gave a better fit (see statistical values in Table 2). The *UV* − *UBVR* fit to this cluster produces acceptable χ_r^2 and *Q*, indicating a cluster only 3.5 Myr old, with mass $\sim 10^5$ M$_\odot$. $E(B − V)$ is 0.34, which corresponds to a visual extinction of $A_V = 1.24$. The observed excesses compared to the best *UV* − *UBVR* model are 0.91, 2.01 and 2.97 mag in *I*, *H* and *K*$_s$, respectively. A similar case is cluster # 6. Here, too, the flux excess is not confined to the NIR part of the spectrum, but also extends into the *I* band, if less dramatically than # 43. In # 6 the *V* − *R* jump is also less pronounced, in agreement with its best estimated age, 8.5 Myr. We found a total of 78 objects affected by flux excess at wavelengths >8000 Å like clusters # 6 and # 43. For these clusters, we have determined physical properties from the *UV* − *UBVR* fit.

After this first look, it is evident that while our single stellar population (SSP) models can successfully model the optical and UV portions of the observed cluster SEDs, they are unable to reproduce the NIR photometry of many of the clusters. This suggests that the models we have used are missing a source of emission which is bright in the NIR.

In Fig. 5 we show how the three different fit types affect the residuals in the SED fits in all filters, for targets with flux excess in the *H* band. The black hatched histograms are the residuals from the *UV* − *UBVRIHK*$_s$ fit relative to the observed data points, $\Delta m = m_{mod} − m_{obs}$, for all the clusters. The residuals in *H* and *K*$_s$ are systematically offset towards positive Δm. In all the other filters the spreads are large, but the residuals are evenly distributed around zero. When the *UV* − *UBVRI* and *UV* − *UBVR* fits were performed, the spread in the residuals of the excluded filters (red
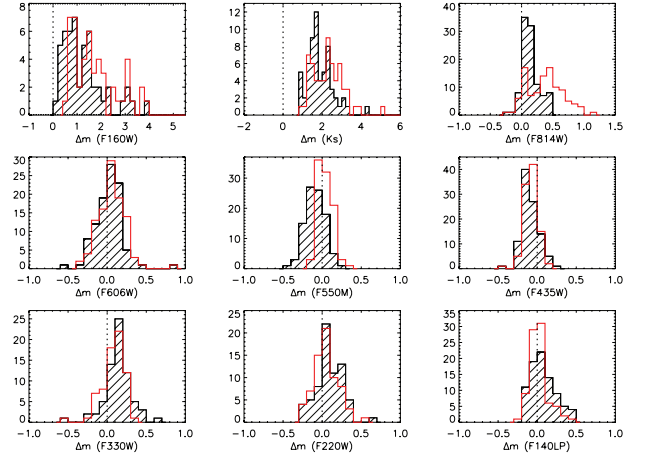

Figure 5. Residuals ($\Delta m = m_{mod} − m_{obs}$) of the χ^2 SED fitting in all the available filters for sources with detected excess in *H*. The hatched black histograms show all these clusters; the histograms with grey borders (red online) are the residual distribution for the same targets but where *I* (if the flux excess is present), *H* and *K*$_s$ have been excluded from the SED fitting. The vertical thick dotted lines indicate zero residuals, i.e. a match between model and observation. The number of objects differs between plots because of the different detection thresholds in each band.

thick histograms for *F*160*W*, *K*$_s$ and *F*814*W*) were even larger. On the other hand, the improvements in the distributions for *R* and blueward filters are clear. The red histogram of the *F*814*W* filter has a secondary peak around zero. This peak is produced by the clusters which do not have any flux excess in *I* band and for this reason fitted by the *UV* − *UBVRI* fit.

In Fig. 6, we show four different colour–colour diagrams for the cluster sample together with the evolutionary tracks by Z01 for different filter combinations. M08 evolutionary tracks with the same metallicity ($Z = 0.004$) are also shown. As pointed out in the previous section, the inclusion of nebular continuum and emission treatment really do make a fundamental difference in the models at the youngest ages, and at all the wavelengths (see differences between the Z01 tracks and those of M08). In particular the broad filters (*F*435*W*, *F*606*W*, *F*814*W* and *F*160*W*) are more affected, with colours changing drastically in the first 10 Myr (see *F*606*W* − *F*814*W*, *F*435*W* − *F*606*W* and *F*160*W* − *F*606*W*). Finally, the colour diagrams which include IR filters also show a difference at older ages (∼1 Gyr) between the two evolutionary models which can be attributed to the better treatment of the AGB phase by M08. In the next section we will show, however, that because of the youth of the clusters in Haro 11, this difference actually only affects a very small fraction of the sample.

The differences in the number of objects in the colour–colour diagrams are due to the different detections limits in each filter. We represent the three cluster subsamples by coloured symbols corresponding to the flux excess. Black filled dots are clusters which do not show any flux excess, red open triangles clusters with observed flux excess in *H* and *K*$_s$; blue open diamonds are clusters with an additional observed displacement in *I*, and cluster with excess in *I* and no detections in the IR bands. In the optical and UV colours (the upper panels of Fig. 6), we see no difference in the distributions of the clusters with and without flux excesses in *I* band. In these panels, many of the clusters can be explained as a young cluster population affected by different values of extinction. Few clusters, affected by red excess, show very red *F*606*W* − *F*814*W* colour (*F*606*W* − *F*814*W* ≥ 1.0 mag) and
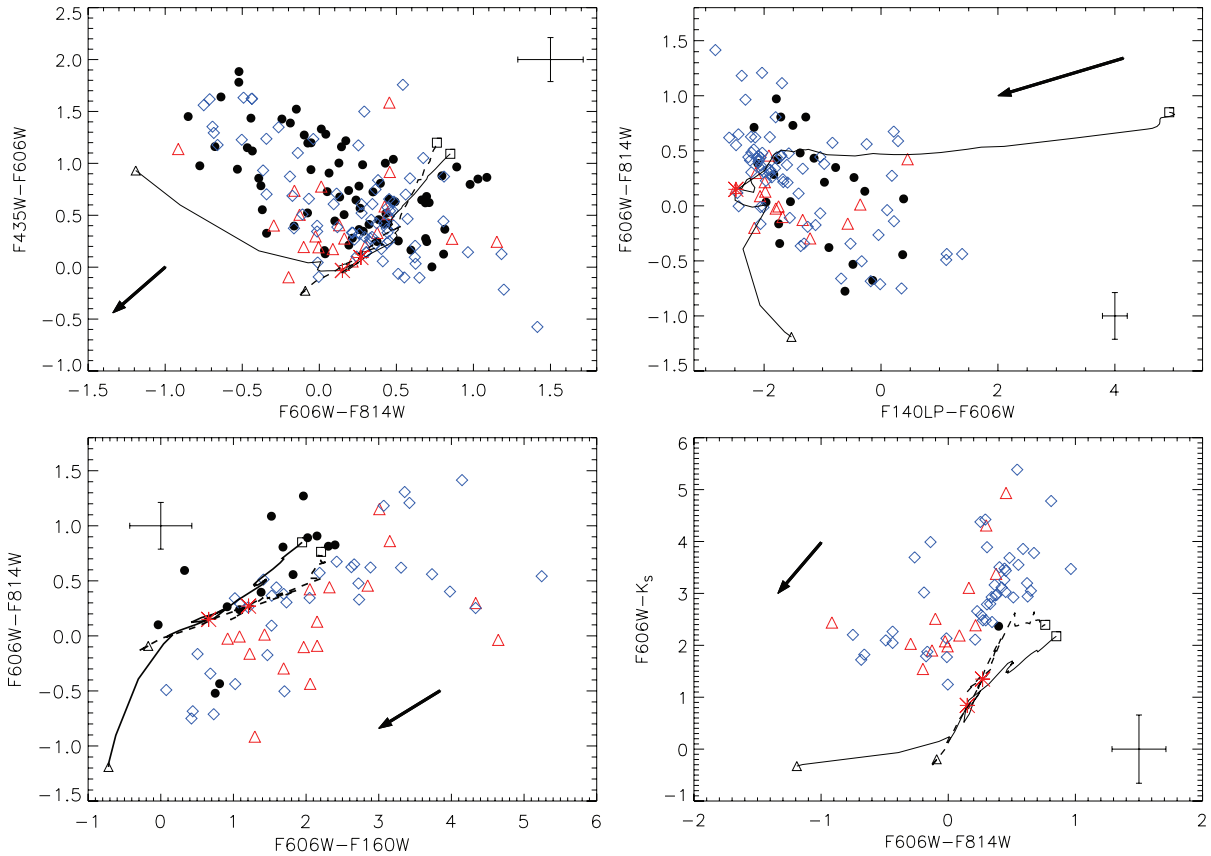
Figure 6. Colour–colour diagrams for the cluster samples. The filled black dots are clusters without a red excess, fitted on $UV - UBVRIHK_s$. The open red triangles are clusters with flux excess in H and K_s and fitted on $UV - UBVRI$, and the blue diamonds denote clusters with excess in all of I, H and K_s, fitted only on $UV - UBVR$. The thick black line shows the predicted stellar evolutionary model according to Z01. The black dashed line is the corresponding M08 model, with $Z = 0.004$. The black triangles indicate the youngest ages included in each model, 0.55 Myr for Z01 and 4 Myr for M08. The red crosses mark the position in the tracks corresponding to 10 Myr and the black squares the end of the tracks at 14 Gyr. In each plot the mean photometric error associated with each object is shown. The arrows indicate direction and displacement produced by an extinction correction of $E(B - V) = 0.3$. The number of objects varies from plot to plot due to different detection limits in each filter.

are displaced relative to the tracks. These clusters and many of the blue open diamonds which show red $F606W - F814W$ colours ($F606W - F814W \geq 0.5$ mag) have UV colours (left-hand column, upper row) consistent with stellar populations younger than 10 Myr ($F140LP - F606W \sim -2$ mag).

Including the IR wavebands (Fig. 6, lower panels) in the colours, changes the situation drastically. Clusters affected by red excess are now displaced from the model tracks by up to 4 mag. Such offsets are impossible to reconcile with the estimated values of extinction. Moreover, several of the sources with red $F606W - F814W$ colour and strong UV emission, which we expect to be very young, have IR colours which lie close to the oldest ages of the model tracks at ~ 14 Gyr. This is again impossible to explain with the current models.

We analyse possible mechanisms producing the excess at the redder wavebands in Section 5. In the next section we will focus on the derived physical properties of the clusters.

4.2.3 Final estimated ages, masses and extinctions

In Figs 7–9 we show our adopted age, mass and $E(B - V)$ distributions for the total cluster sample, with 187 objects (black hatched histograms). In this final sample, only in 21 per cent of the cases we determined cluster properties using three filters, while the
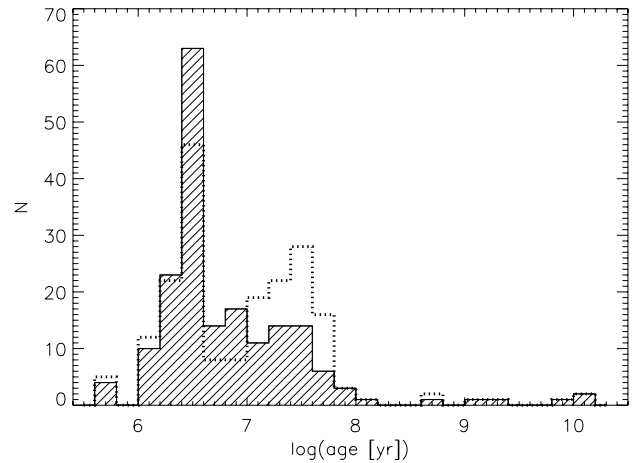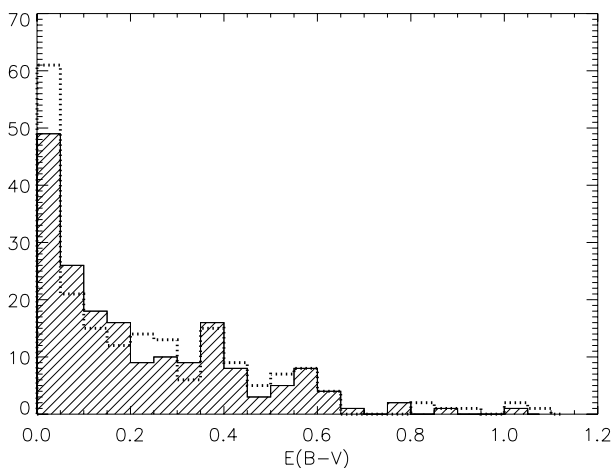

Figure 7. Final age distribution of the SC population (black hatched histogram). The dotted overplotted distribution shows the age distribution if the SED is fitted over the whole $UV - UBVRIHK_s$ range, without taking the red excess into account.

53 per cent had detection in at least five or more bands. The cluster properties of the targets affected by a red excess have been obtained from the fit to the blue side of the SED spectra. For comparison we overplotted the corresponding distributions (dotted histograms)
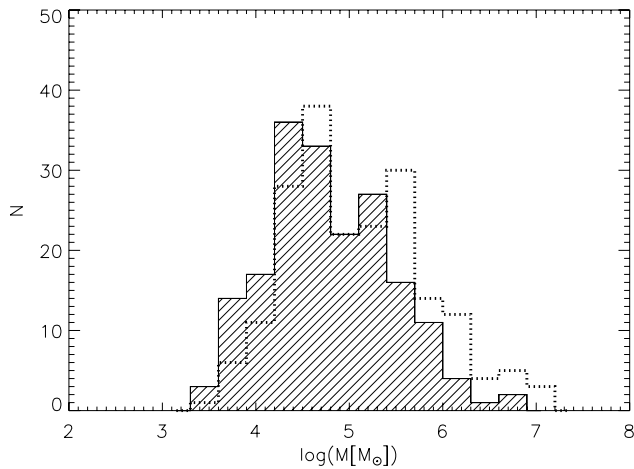
Figure 8. Final mass distribution (black hatched histogram) of the SC population. The dotted overplotted distribution shows the masses obtained for the clusters if the SED is fitted over the whole $UV - UBVRIHK_s$ range.


Figure 9. Final extinction distribution (black hatched histogram) of the SC population. The dotted overplotted distribution shows the extinctions obtained for the clusters if the SED is fitted over the whole $UV - UBVRIHK_s$ range.

produced by a $UV - UBVRIHK_s$ fit to the entire sample of clusters. The red excess clearly introduces a systematic offset in the estimates of all the derived parameters. When all the filters are included in the fit, clusters with a red excess appear to be older and more massive than their UV–optical photometry alone would indicate. What happens is that when we attempt to fit the NIR filters affected by flux excess, the best model choices are old stellar populations in which lower mass stars dominate the light. This affects the mass estimation because the M/L ratio increases with age: for the same luminosity, older clusters are also more massive. For example, cluster # 43 (Section 4.2.2 and Fig. 4) shows that even the excess in I band (at ~ 8000 Å) has important consequences for the estimation of the cluster ages and masses.

So far, the filter $F814W$ is one of the most used in the photometric analysis of the cluster populations in extragalactic environments. Because the flux excess in this filter is not as dramatic as in the IR filters, it may go unnoticed when IR data are not available. Indeed, this affected our own initial analysis of Haro 11's cluster population (Hayes et al. 2007). In that paper, the cluster age distribution showed the same double peak as we have shown here where no

correction for red excess is performed (dotted histogram in Fig. 7). Extinction estimates, on the other hand, tend to be more sensitive to the $UV - U$ fluxes and are therefore not affected by red excess.

The cluster population in Haro 11 appears to be very young (Fig. 7). The present starburst phase started less than 40 Myr ago with a peak at the extremely young age of 3.5 Myr. Only 16 clusters have estimated ages older then 40 Myr and of these, half have an age >100 Myr. The age distribution is in agreement with the estimated burst duration, $\tau_b = M_{burst}/SFR = 35$ Myr found by Östlin et al. (2001), where M_{burst} is the total mass contained in the burst and SFR. They estimated an upper limit age for the present burst of 35 Myr, taking the SFR from the total Hα luminosity, uncorrected for extinction. The age peak at 3.5 Myr is consistent with the young stellar population (age < 5 Myr) which Galametz et al. (2009) identified as responsible for the hard radiation field inferred from the observed ratio of [Ne III]/[Ne II] $= 3.2$ in the galaxy's integrated mid-IR *Spitzer* Infrared Spectrograph spectrum. With about 130 clusters younger than 10 Myr, Haro 11 represents a unique opportunity to investigate the cluster formation process and evolution at the youngest phase in starburst systems. In recent reviews, Larsen (2009b) and Lada (2010) pointed out that clusters younger than ~ 5 Myr are still partially embedded and affected by several magnitudes of internal extinction due to the remains of the GMCs in which they formed. In Haro 11, the estimated extinction distribution is quite wide with a peak at $E(B - V) \sim 0.0$ and an extended tail down to at least 0.6 mag (Fig. 9; corresponding to $0.0 \le A_V \le 2.2$ mag). The few cases with $E(B - V) \ge 0.8$ mag have $2.9 < A_V < 3.7$ mag.

In Fig. 10 we show how the derived extinction changes as a function of cluster age. For ages between 1 and 3.5 Myr the extinction range is wide. Almost all the clusters with $E(B - V) > 0.4$ ($A_V > 1.5$) mag are located in this age range, but the number of clusters with lower extinction is not negligible. This observed spread shows the complexity of the cluster formation process and the gradual dissolution of the parent clouds. A correlation might be expected between the extinction of clusters younger than 5 Myr and their masses, but we found no clear trend. This lack of correlation could indicate that we have underestimated of the mass of partially embedded clusters. If this is the case, then we should consider the
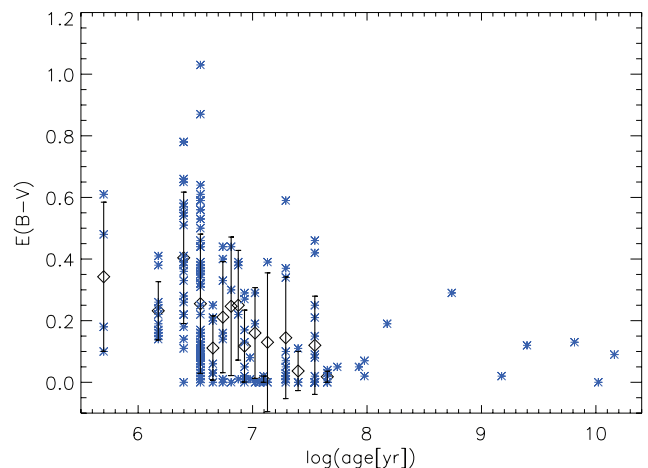
Figure 10. Extinction versus cluster age. The small grey (blue online) asterisks are the extinction as a function of the age for each cluster. The black open diamonds indicate the mean value at each age step in the model, as long as at least three objects are contained in the bin. The associated error bars are the 1σ uncertainties.

estimated masses at very young ages as a lower limit to the real values. At older cluster ages (>5 Myr), we can see in Fig. 10 that extinction tends to decrease as a function of the age, although the deviations are large. Moreover, previous studies have shown that the galactic environment is quite complex (Bergvall & Östlin 2002; Hayes et al. 2007), and the mean extinction in the galaxy is patchy. Some regions are apparently free from extinction while in others thick dusty clouds and filaments are apparent (see Fig. 1). Finally, we noted that similar trends between cluster ages and extinctions have also been observed in the Antennae system (Mengel et al. 2005) and in M51 (Bastian et al. 2005).

The clusters are quite massive. More than half of the targets have masses between 10^4 and 10^5 M$_\odot$. In Haro 11 we have found around 60 estimated SSCs (clusters with the masses $>10^5$ M$_\odot$), seven of which have masses larger than 10^6 M$_\odot$. The two knots, B and C, have masses $\sim 10^7$ M$_\odot$. The fit for knot C is poor, however, and its estimated age, mass and extinction have not been included in Figs 7–9. We present a more detailed analysis of these two regions below. Only ~ 20 clusters have masses below 10^4 M$_\odot$, though this small number is affected by the detection limits we have imposed on the available data.

In Fig. 11 we show estimated masses as a function of our derived cluster ages. The lines indicate the predicted detection limits using the Z01 stellar evolutionary model, for the corresponding magnitude limits (see Table 1) as indicated in the plot. Detections below these thresholds are highly unlikely. All the clusters in the plot have been detected in R and I bands (used to make the initial catalogue; Section 3.3), and at least in one other filter. While the clusters affected by red excess have a wide mass range, we noted that all the most massive clusters ($M \geq 5 \times 10^5$ M$_\odot$) younger than 40 Myr appear to be affected by at least some flux excess in the NIR. We detected no clusters older than 40 Myr with any red excess. Six objects with masses around 10^5 M$_\odot$ and ages greater than 500 Myr have properties similar to more evolved globular clusters, as in the MW.

Curiously, even though restricted detection limits allow us to detect very young clusters (1–3 Myr) with masses around 10^3–10^4 M$_\odot$, we see almost none in this range of age and mass. This peculiar phenomenon could be interpreted in different ways. (1) Low-mass clusters $<10^4$ Myr are still embedded in their parental

clouds so they are not 'visible' in optical wavebands. (2) At the distance of Haro 11, sources may be blended. Indeed, we expect clusters to form in complexes rather than singly (Elmegreen 2010). If this is the case, some of the more massive observed clusters may in reality be clumps of several low-mass clusters. (3) The model, in particular its handling of the nebular component, has limitations which may lead to objects at 1–3 Myr having their ages overestimated. We will return to these three points in Section 6.1. For the moment, we note that none of the three explanations excludes the others and all three could account for the apparent absence of very young low-mass clusters.

Finally, we have investigated the two most active star-forming regions in the galaxy, knots B and C (Fig. 1). We performed aperture photometry on the two central regions in the same way done for the point-like clusters even though these two regions appear extended. Knot C is more reminiscent of a nuclear cluster than a point-like SC. Dusty filaments appear at the two sides of the central region in a cone shape. Hayes et al. (2007) pointed out that knot C is the brightest source in the UV, with strong Lyα emission from its centre, possibly indicating that star formation in knot C is still ongoing. Knot B appears obscured by filamentary dust clouds passing through its central region. It is not clear from our images whether this central region is composed of a single massive object or several clusters in a clump similar to the ones observed in the nearby starburst galaxy M 82 (Melo et al. 2005; Westmoquette et al. 2007). Knot B is the most massive cluster-like object after C. Both knots appear affected by the red excess (see Fig. 12) and are very massive objects. The best fits were obtained with a $UV - UBVRI$ fit for both clusters. The physical properties of B and C are summarized in Table 3. As showed by the χ_r^2 value, the fit to knot C is poor so its properties have to be considered as an approximation. We have obtained spectra of these knots with VLT/X-shooter which will be the subject of a future paper (Cumming et al., in preparation). Here we exclude knot C from our final analysis of the cluster population properties.

4.3 Can a different extinction law give different results?

Could a different extinction law have an impact on our estimates of the physical properties of the clusters? To answer this question we performed a second χ^2 fitting run, this time assuming a Large Magellanic Cloud (LMC) dust extinction law (Fitzpatrick 1986; Misselt, Clayton & Gordon 1999). Both the LMC and Calzetti (Calzetti et al. 2000) laws have been obtained from different environments and physical conditions. The Calzetti extinction law (Calzetti et al. 2000) was derived from the integrated spectra of several starburst galaxies, so it describes the total extinction affecting a galactic environment and produced by different mechanisms. Since dust is in general mixed in galaxies, different optical depths are probed as a function of wavelength, and the emerging 'Calzetti law' results from the combination of this effect and the underlying extinction law. On the other hand, the LMC law was determined from the spectra of stars located inside and near the 30 Dor cluster and reproduces the local extinction produced by a molecular dust cloud on single stars, in which case the dust can be accurately treated as a screen. The situation in Haro 11 may, at this distance, be intermediate to these two cases, and most results presented assume the Calzetti law. However, it was important to assess whether the LMC law produces different results. Comparing the outputs of the two runs, we noted the following. (1) The values of χ_r^2 obtained with the LMC law are similar to the Calzetti law results and show no improvement in the fit. (2) The clusters still display pronounced red excesses. In Figs 15, 14 and 13 we have plotted the recovered
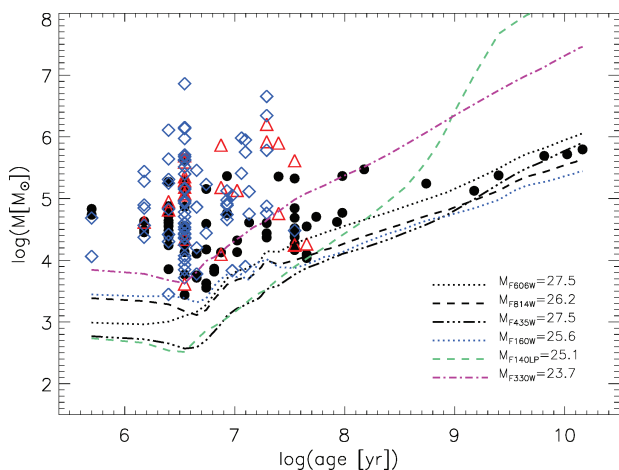
Figure 11. Ages versus masses for the SC population. Estimates from $UV - UBVRIHK_s$ fits are shown as filled black dots, while estimates from $UV - UBVRI$ fits and $UV - UBVR$ fits are shown as red triangles and blue diamonds, respectively. The lines are the expected detection limits in various filters (see the labels) according to our stellar evolutionary models.
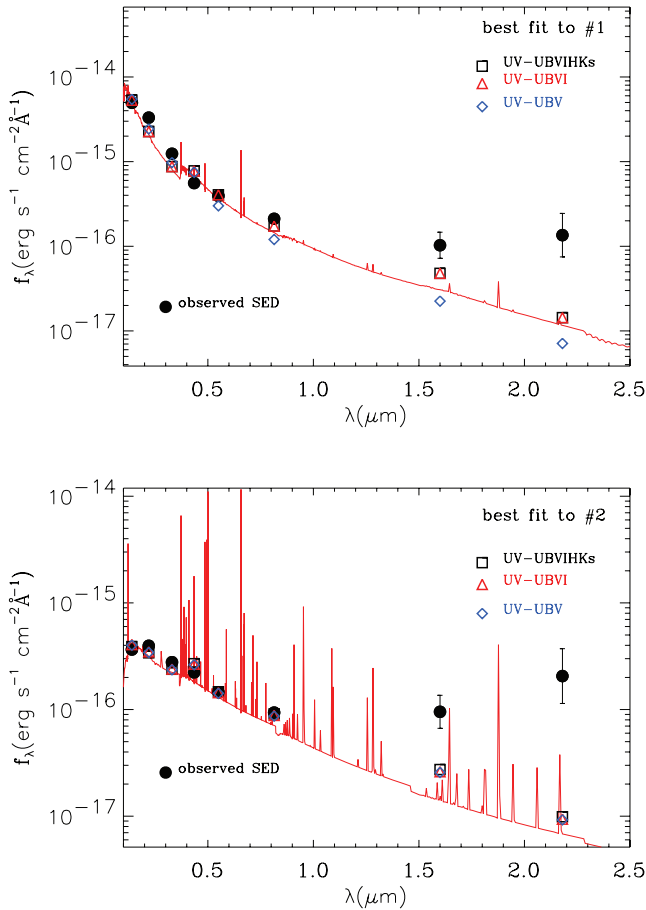
**Figure 12.** SED analysis of the two knots, C (# 1, above) and B (# 2).

Table 3. Ages, masses and extinctions for the two star-forming regions B and C.

ID	χ_r^2	Age (Myr)	Mass ($M_\odot$)	$E(B-V)$
B	3.3	3.5	8.35×10^6	0.38
C	36.0	9.5	1.36×10^7	0.06

extinction, mass and age distributions obtained using the Calzetti (green hatched histograms) and LMC (dotted histograms) laws. The use of a different extinction law does not have any significant impact on the age distribution of the clusters. Only a few clusters have discordant age estimates, as we show in the inset of Fig. 13. On the other hand, about one-third of the clusters fitted with an LMC extinction law appear to have higher estimated masses (Fig. 14). This trend in the estimated mass can be explained by the recovered extinctions when the LMC extinction law is used. Comparing LMC and Calzetti $E(B-V)$ distributions (Fig. 15), we see that a considerable number of objects with Calzetti $E(B-V)$ in the range 0.1–0.6 appear distributed in a long tail towards higher extinction values. In particular, the quantitative difference in visual extinction A_V can differ almost a factor of 2, depending of which extinction law is used (see the inset in Fig. 15). This in turn means that objects affected by higher extinctions have higher estimated masses. While we cannot draw any definitive conclusion on the choice of the extinction law, it is clear that a considerable fraction of our recovered extinctions and masses can depend on the adopted extinction law. Such uncertainties should be taken into account when cluster prop-
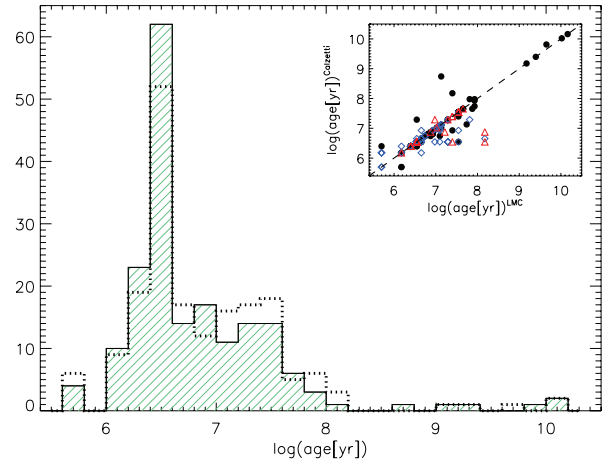
Figure 13. Recovered age distributions using Calzetti (green hatched histogram) and LMC (dotted histogram) extinction laws. In the inset, we compare for each cluster the age estimated with the two extinction laws. The different symbols are the same as in Fig. 11.
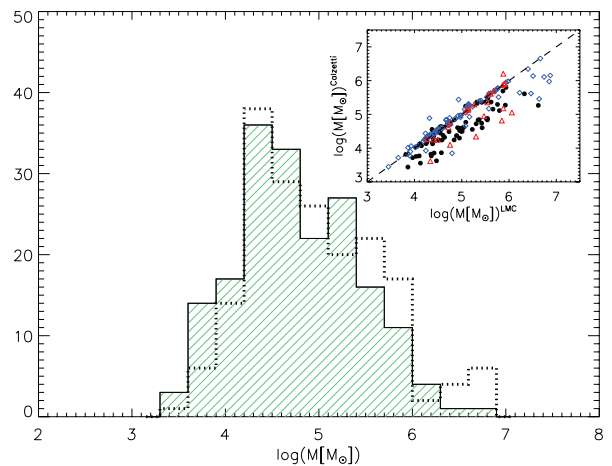

Figure 14. Recovered mass distributions if a Calzetti (green hatched histogram) or an LMC (dotted histogram) extinction law is used. The inset shows a direct comparison is shown between the recovered masses for the two different fitting runs. The different symbols are the same as in Fig. 11.

erties are estimated. Age estimates, on the other hand, appear to be robust.

4.4 Testing the SED fit results with Monte Carlo simulations

The outputs recovered by the SED fitting technique are connected to the stellar evolutionary models we used. In order to estimate the uncertainties in our recovered ages, masses and extinctions, we used Monte Carlo methods to simulate a fully sampled population of clusters which resembles the population we observe in Haro 11. The initial sample contains clusters with three different mass values (10^4, 10^5 and $10^6\,M_\odot$) for each of 51 age step of the evolutionary model, and three extinctions [$E(B-V) = 0.05, 0.3$ and 0.5], yielding a total of $3 \times 51 \times 3 = 459$ clusters.

For each cluster, we use the spectral synthesis models to calculate its apparent magnitude in all the nine filters for the mass, age and $E(B-V)$ in question. To these ideal magnitudes that perfectly match the model prediction, we add random photometric errors in accordance with the observed magnitude–error relation in each filter and assuming a Gaussian error distribution. In this way we simulated
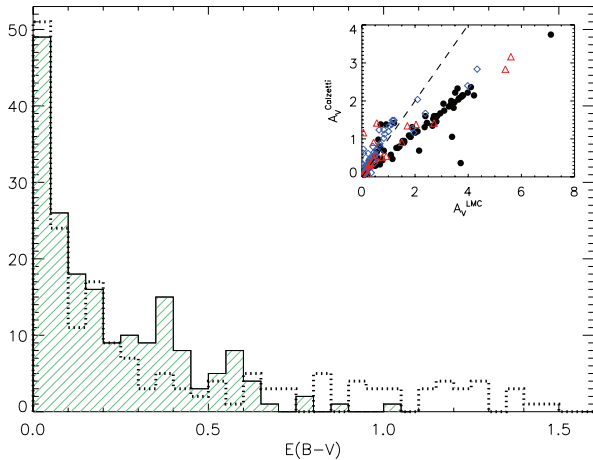
Figure 15. Recovered extinction distributions using Calzetti (green hatched histogram) and LMC (dotted histogram) extinction laws. The inset shows for each cluster the corresponding visual extinction, A_V, recovered in the two cases. The different symbols are the same as in Fig. 11.

1000 realizations of each cluster, then fitted them with our SED tool and compared the input to the output for 1000 hypothetical clusters.

All the 1000 realizations of each cluster were fitted with the same χ_r^2 fitting program using an $UV - UBVRIHK_s$ fit, an $UV - UBVRI$ fit and a $UV - UBVR$ fit in turn. The median and quartiles of the distributions are considered to be the estimated output age and associated uncertainties, respectively, for each cluster. In Fig. 16 we show how the recovered age of an object and its uncertainty changes depending on the mass and extinction of the object, and the type of fit. From the initial cluster sample, combinations of age, mass and extinction which resulted in a cluster with apparent magnitude $m_R > 27.5$ mag was excluded from the analysis. Looking at the two panels of Fig. 16 we can see that this cut in luminosity appears as an incomplete sampling at older ages. In general, for the same mass, clusters with lower extinction are better fitted. The higher the cluster mass, the smaller the uncertainties at all ages and with respect to the reddening. For higher values of the reddening, input ages of ~10 Myr tend to lead to older output ages (and between 100 Myr and 1 Gyr) with a tendency to underestimate the output ages. This last effect is less important for higher masses and for lower extinction.

To test for systematic effects of our three different SED fits, we checked and compared the three sets of recovered ages for the same mass and extinction distributions. In Fig. 16, we show two of the three SED fits. As expected, if fewer filters are available, the properties derived from the observed SED become more uncertain, and we see the quartile error bars get wider. The median of the distributions, on the other hand, are not affected except at two critical ages, around 10 and 100 Myr. These age ranges correspond to particular features of the synthetic stellar population model. There is a loop in the modelled colours at ages between 10 and 40 Myr which makes it difficult to distinguish between different age steps. At intermediate ages, around 100 Myr, the tracks are parallel to the reddening vector (see Fig. 6, upper left-hand panel) and clusters could be fitted equally well with younger ages and higher extinctions. We found no other evidence of systematics introduced by our analysis. This can be seen also in the plots in Fig. 17, in which we compare the input age distribution (histogram with thick red border) of the simulated cluster population with the recovered one (black hatched histogram) derived from the three fit ranges. Once

more we exclude clusters with $m_R > 27.5$ mag from the analysis. When all the filters are included in the $UV - UBVRIHK_s$ fit, the input and output distributions differ little. With a $UV - UBVRI$ fit the disagreement between the input and output distributions is more evident with a tendency to overpopulate the age bin around 10 and 60–80 Myr. The exclusion of the I band in the $UV - UBVR$ fit moves the peak from 10 Myr to 30 Myr, and the spurious peak a 60–80 Myr remains. In Fig. 7 we see that the introduction of a subsample of clusters analysed with $UV - UBVRI$ or $UV - UBVR$ fits produces a peak in the age distribution at 3.5 Myr [log(age) = 6.3], populated by objects from older age bins, like 35 Myr. In the distributions of the simulated cluster sample we used the same age bin size as in Fig. 7. None of the fits performed introduces any displacement to or spurious peak at 3.5 Myr. For this reason, we are quite confident about the robustness of our estimates.

5 WHAT IS THE CAUSE OF THE RED EXCESS?

Following our analysis of the cluster photometric and physical properties, we address the question of what causes the excess of the observed fluxes longward of 8000 Å with respect to the synthetic evolutionary models. Clusters with red excesses have also been observed in other galaxies (Whitmore & Zhang 2002; Cresci, Vanzi & Sauvage 2005; Reines et al. 2008a; Reines, Johnson & Hunt 2008b; Fernández-Ontiveros, Prieto & Acosta-Pulido 2009). They are typically very young and bright at IR wavelengths, and appear to be subject to significant dust extinction at optical wavelengths. Their location in colour–colour diagrams tend to be offset towards both red $V - I$ and $V - K$ colours. An observed flux excess in I band was found by Reines et al. (2008a) in the young clusters of the galaxy NGC 4449. A subsequent spectroscopic analysis of two of these clusters (Reines et al. 2010) revealed that the flux excess could be explained if a contribution from nebular continuum and emission lines were taken into account. This explanation can be excluded in the case of the I-band excess in Haro 11's clusters since our models already include both nebular continuum and emission lines.

Thanks to the large number of clusters with red excesses in Haro 11, we were able to check possible correlations between the magnitude of the excess at $\lambda > 8000$ Å and the cluster physical properties. First of all, we looked at the position in the galaxy of clusters affected by a red excess (Fig. 18). They are mainly located in the three starburst knots, as one might expect from their young ages. Comparing Figs 1 and 18 shows that many clusters with flux excesses are located close to dusty regions. Nevertheless, we found no clear relation between the measured cluster excesses and the corresponding estimated extinctions (Fig. 19, right-hand column).

We have looked for further clues to the red excess by comparing the deviations from the best SED fits (Δm) with the derived properties of age, mass and extinction. In Fig. 19 we plot the measured flux excess in I, H and K_s against the recovered ages, masses and extinctions of the clusters. We see no correlation between the strength of the displacement and any of these properties. The only correlation with age, visible in Fig. 11, is the absence of clusters affected by a red excess with ages older than 40 Myr. This result may however be biased by the small number of objects in the older age bins. In summary, the lack of any clear relations seems to indicate that the red excess could be produced from different mechanisms in different clusters.

As first discussed by Reines et al. (2008a), different mechanisms could cause the red excess of such young ages. For clusters younger than 5 Myr, a possible explanation for the observed I-band excess is the extended red emission (ERE) phenomenon. ERE has been
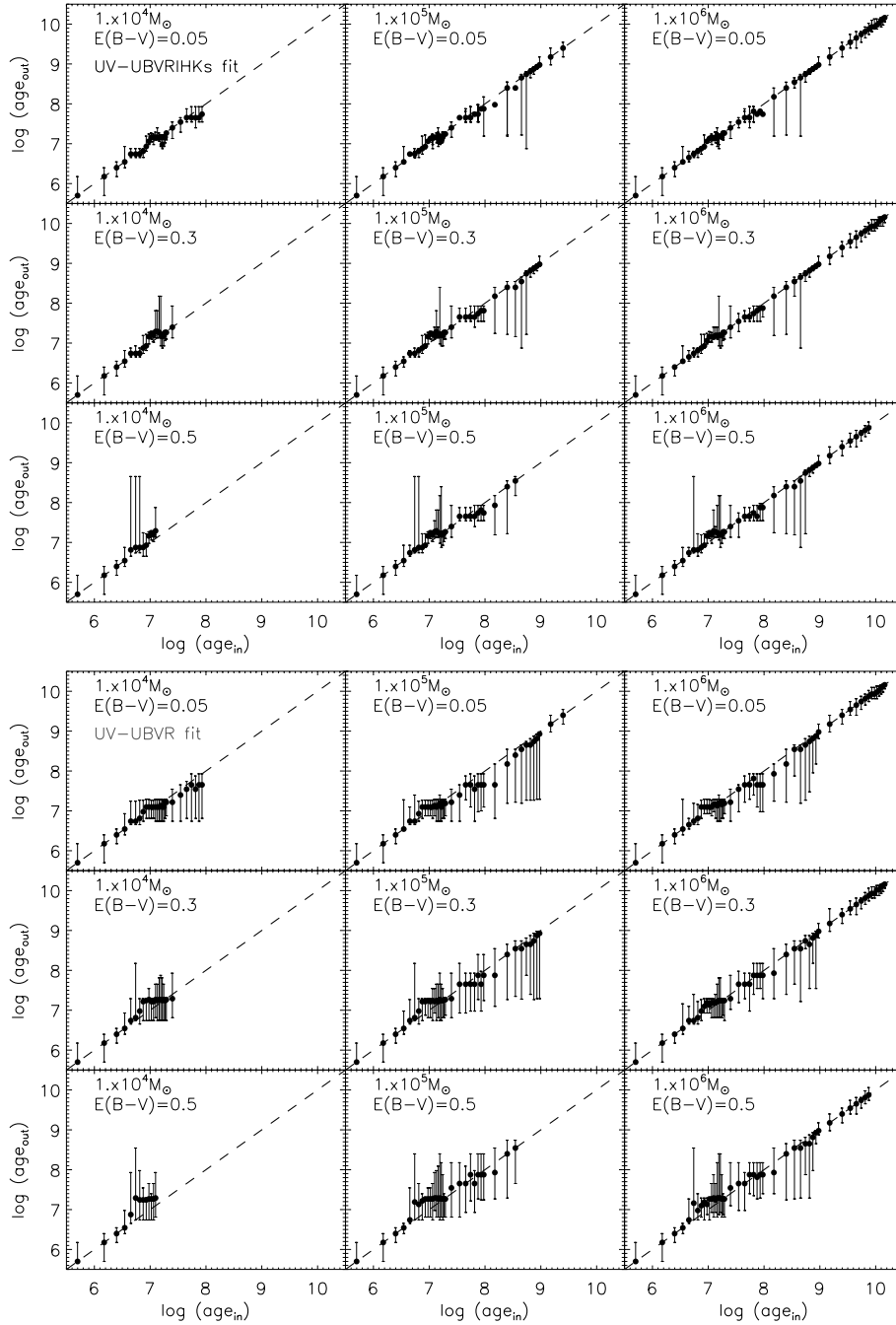
Figure 16. Recovered ages as a function of the input ages for different values of masses and extinctions, as specified in the labels. Nine combinations of mass and extinction are shown for two of the fit ranges $UV - UBVRIHK_s$ (top) and $UV - UBVR$ (bottom). The dashed lines mark where input and output ages are equal. The output ages are the median values of the 1000 realizations of each cluster and the error bars are the quartiles of the distribution. Simulated clusters with apparent magnitude $m_R > 27.5$ mag have not been included in the analysis. This cut in magnitude is reflected in the plots as incompleteness of the full age sampling.

observed in a wide range of environments, among them star-forming regions (see Witt & Vijh 2004 for a review) and it affects mostly optical and near-IR wavelengths, between 7000 and 9000 Å. The effect is expected to be strong in presence of strong UV radiation fields (as Haro 11 has been shown to possess; Galametz et al. 2009) mainly produced by the most massive stars in the clusters. However, as we have noted, this mechanism cannot explain the excess in the IR, so a different physical process needs to be considered.

Clusters younger than 5 Myr are still partially embedded in the original dust cloud. At this stage the complexity of the cluster environment and the uncertainties in the used models are quite large. Hot dust emissions can produce a 'rise' at IR wavelengths. The strong UV radiation field produced by the most massive stars in the cluster is expected to be absorbed by dust grains, which eventually re-emit photons at IR wavelengths depending on the size and temperature of the grains. Since Haro 11 has a total far-infrared
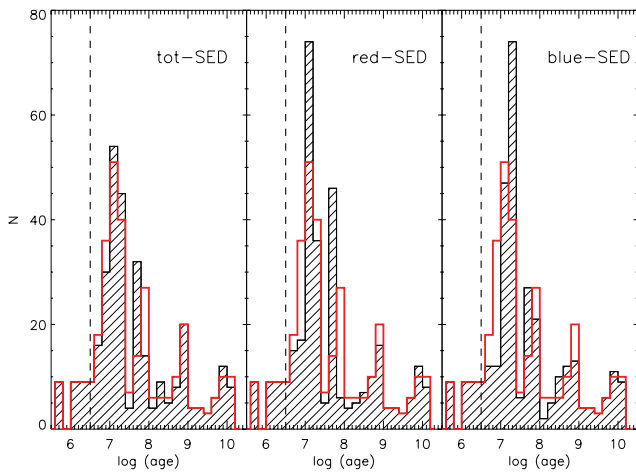
Figure 17. Recovered age distributions (black hatched histograms) of the three sets of fits. From left- to right-hand side, the recovered age distributions for $UV - UBVRIHK_s$, $UV - UBVRI$ and $UV - UBVR$ fits. The red histograms show the input ages of the simulated sample of clusters.
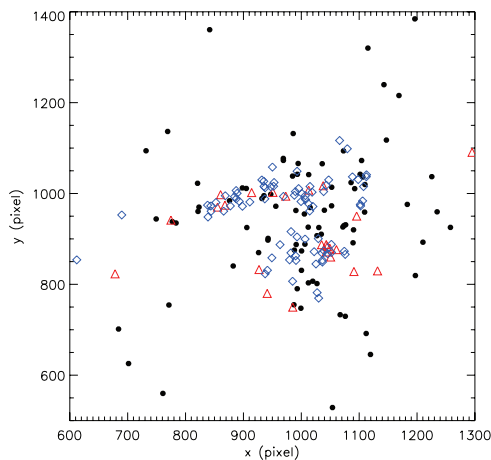
Figure 18. Position in the galaxy of the three subsamples of clusters. The normal clusters are labelled as filled black points. Clusters with flux excess in H and K_s are denoted by red triangles; clusters with excess also in I band are the blue diamonds.
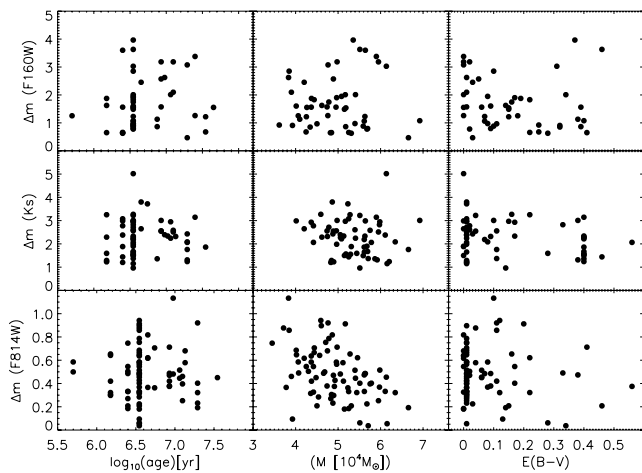
Figure 19. Residuals of the χ^2 fits in I (bottom), K_s (middle) and H (top) versus the estimated ages (left-hand column), masses (centre column) and extinctions (right-hand column).

(FIR) luminosity that qualifies it as a LIRG, such processes are undoubtedly working in the galaxy (Galametz et al. 2009; Smith & Hancock 2009). Similar explanations were first suggested by Reines et al. (2008b) to explain the red excess they observed in the SSCs of SBS 0335−052. New fits to those clusters (Adamo et al., in preparation) show that the excesses in these clusters can be explained by nebular emission, a possibility which was not addressed by Reines et al. (2008b). On the other hand, at such young stages, it is possible that the clusters have two stellar components, one of which has been able to shed its dust envelope and contribute to the UV–optical emission while the other is still embedded in the star-forming cloud and still highly extinguished. These embedded stars are pre-main-sequence objects and young stellar objects (YSOs) still surrounded by circumstellar discs that can produce this IR-bright component. Modelling is required in order to estimate how massive should be the second stellar component in order to produce such large displacements in H and K_s bands. Moreover, the presence of an embedded stellar population contributing only in the IR would imply an incorrect mass estimation for the clusters.

The UV radiation field is expected to soften after a few Myr as the most massive stars evolve and finally explode as supernovae. This means that in clusters older than 5 Myr the I-band excess cannot be explained by the ERE. We also expect that for ages >5 Myr, the embedded phase is over and YSOs and pre-main-sequence stars have evolved so that they do not contribute anymore to the IR fluxes.

Two further effects could explain the presence of a NIR excess in older clusters. (1) Blends of two or more clusters may well be present in our data. The pixel size at distance of Haro 11 corresponds to ∼9 pc. If, for example, an older cluster is seen in the line of sight towards a very young, embedded cluster, the cluster behind would only be visible at IR wavelengths, while the estimated age and mass are for the UV–optical bright cluster in front.

(2) Uneven IMF sampling in less massive clusters can also affect the expected NIR flux. Studies of the evolution of the stellar isochrones (Maíz Apellániz 2009, among many others) have shown that red supergiants (RSGs) dominate the SC light in red and near-IR wavelengths as early as 6 Myr. Z01 models are constructed by integrating the contribution to the cluster's light from all the stars populating a well-sampled IMF, normalized with respect to the mass of the cluster. This method is, however, valid only if the stellar population has a total mass of at least $10^6 \, M_\odot$, otherwise uneven sampling introduces important changes in the colours of the clusters. In fact, the IMF describes a probability distribution of the mass at which stars form. This means that, in nature, the IMF sampling is a purely stochastic event. For clusters with masses not large enough to fully sample the IMF, the colours of the clusters are dominated by fluctuations around the expected values (see Lançon & Mouhcine 2002; Cerviño & Luridiana 2004; Fouesneau & Lançon 2009 and Lançon & Fouesneau 2009). At cluster ages between 6 and 60 Myr, RSGs dominate the light at red and near-IR wavelengths. If the observed cluster happens to have a larger number of RSGs than that predicted by the model, this would be seen as an excess in the observed flux at $\lambda > 8000$ Å. Simulated clusters with stochastic IMF sampling deviate from the expected evolutionary tracks by as much as $1.0 < V - H < 5.0$ ($0.5 < V - I < 2.0$), compared to the expected $0 < V - H < 1$ ($-1.0 < V - I < 0.3$) colours (M. Fouesneau, private communication).

Finally, a bottom-heavy IMF could in principle explain the IR excess over all the age range. However, it is difficult to imagine why only a fraction of the clusters would manufacture stars with a different IMF. A recent review by Bastian, Covey & Meyer (2010)

shows observational evidence for a universal IMF shape in different galactic and extragalactic environments. Finally, the total stellar mass necessary to produce such an excess would be very high and unphysical for 'normal' clusters.

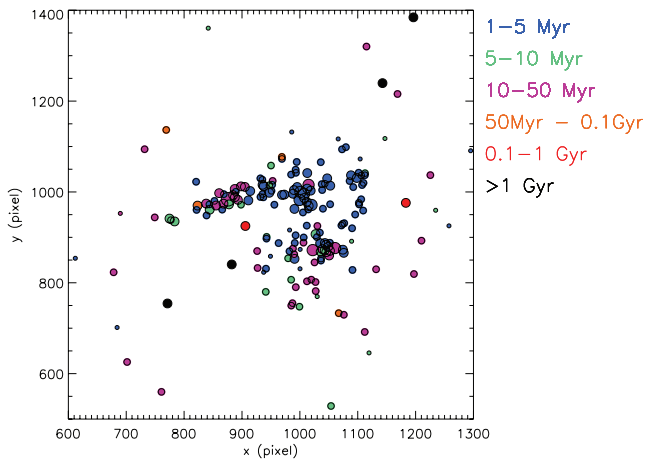# 6 GLOBAL STARBURST PROPERTIES AND EVOLUTION DERIVED FROM THE STAR CLUSTERS

In Fig. 20 we show the position of the clusters in the galaxy as a function of their estimated ages (colours) and masses (circle sizes). The youngest clusters (in blue) are located mainly close to knot B. The locations suggest a starburst propagating from the older regions C and A towards knot B. Older clusters are located throughout the main burst regions. The clusters outside the main starburst appear to follow a spiral arm-like distribution, but in the absence of information on the three-dimensional distribution we do not explore this possibility further.

6.1 The cluster luminosity function and the fraction of missing clusters

In Fig. 11 we pointed out a deficit of low-mass clusters in the age range of 1–3 Myr. Using our SSP model, we estimated that clusters at these ages and masses should have apparent magnitude in I band in the range 23.0–26.0 mag. In Section 3.2, we have showed that in the crowded, most active star-forming regions where we expect to find mainly young clusters, detection limits went below 90 per cent already at ∼25 mag. Therefore it is possible that a fraction of low-mass clusters is lost because they are heavily embedded and fall below the detected thresholds imposed by the available data. Blending may also affect our sources in that we are not able in some cases to resolve single clusters. We consider it very unlikely that the missing clusters have already been destroyed (so-called 'infant mortality'; Lada & Lada 2003). For help with this issue, we decided to investigate the CLF. We define the CLF as

$$dN(L_i) = BL_i^\alpha dL_i, \tag{1}$$

where L_i is the luminosity of the clusters in a given waveband i, and B is a constant. In order to determine the slope, α, we fit a linear relation in log–log space,
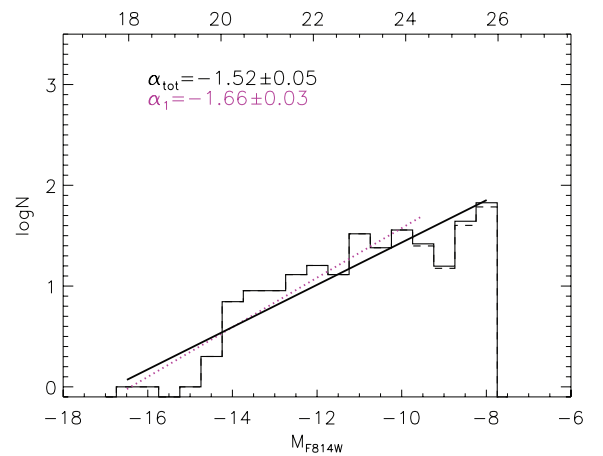
$$\log N(L_i) = AM_i + D, \tag{2}$$

with the variable A related to α according to

$$A = -0.4(\alpha + 1). \tag{3}$$

In our specific case we excluded the R filter ($F606W$) because it is heavily contaminated by Hα emission at the youngest ages, yielding a shallower CLF. The $F814W(I)$ band is instead more suitable for constructing the CLF. As we stated in Section 3.1, 563 objects were detected in both I and R bands. To avoid uncertainties due to underestimates of the completeness, we used only clusters detected above the 90 per cent completeness limit in I (< 26.5 mag), giving a total of 304 objects. In Fig. 21 we show the resulting CLF for the I band in absolute magnitudes, adopting a distance modulus of $M - m = 34.58$. The thick black line is the best fit to the total distribution, corrected for incompleteness. The obtained slope $\alpha_{\rm tot} = -1.52 \pm 0.05$, below the typical observed value, $\alpha \sim -2$. Fitting a double power law produces small difference between the slope in bright and fainter bins, so that does not improve the fit. However, we noted in Section 3.2 that in crowded regions the 90 per cent completeness limit is reached already at ∼25.0 mag. We therefore performed a conservative fit including only objects brighter than 25.0 mag. The recovered slope is steeper ($\alpha_1 = -1.66 \pm 0.03$) but still not close to -2. We also tried to construct an extinction-corrected CLF, using only clusters with known extinction. The recovered slope of the distribution, $\alpha = -1.64 \pm 0.02$, was still unchanged.

It is known that crowding and projection effects can flatten the slope of the LF (Larsen 2002). At the distance of Haro 11, and with a pixel resolution of ∼9 pc in the $F814W$ HST filter, some of the clusters are resolved. With an aperture radius of 4 pixels, our photometry was carried out in a region of diameter ∼72 pc, much larger than typical cluster diameters (5 pc). Bright detections may therefore be the result of overlapping sources. By substituting in equation (3), $\alpha = -2$ and the constant D, given by the assumption that the number of objects in the third bin is correct (we exclude the two brightest objects, which are knots B and C), we made a rough estimation of the missing fraction of clusters using equation

Figure 20. Spatial distribution of the SCs in Haro 11. The different circle sizes correspond to four mass ranges ($M \geq 10^4$, 10^4–10^5, 10^6–10^7 and $>10^7$ M$_\odot$). The age ranges are defined by colours as indicated in the legend.

Figure 21. Observed CLF in the $F814W$ filter with (solid line histogram) and without (dashed line histogram) corrections for incompleteness. The plot shows both absolute and apparent magnitudes. The thick black line shows the best fit to the completeness-corrected distribution; the slope $\alpha_{\rm tot}$ is indicated in the plot. Finally, the dashed line (magenta online) is the best-fitting line to the distribution with lower magnitude limit set to 25.0 mag (the 90 per cent completeness limit for cluster inside the crowded region; see Section 3.2). The slope α_1 is labelled in magenta.

(2). This leads to an estimate of 85 per cent of objects missing in our analysis. However, this fraction seems unreasonably high and impossible to reconcile with the number of detected clusters and the output of our completeness test. While we are certain that blending affects our data, we cannot give a quantitative estimate of the effect on the CLF. Moreover, some of the low-mass clusters with ages between 1 and 3 Myr are still in the embedded phase and may fall below the optical detection limits due to extinction. Interestingly, in our group's previously published CLF study of SCs in another BCG, ESO 338−IG04, by Östlin et al. (2003), the slope found was −1.8 ± 0.15. This galaxy lies close enough (∼37.4³ Mpc) for blending between systems not to be an issue. However, the steepness of the CLF is still below the expected value. It is possible that the physical environment in BCGs differs from other late-type galaxies, perhaps related to their status as merging and interacting systems. It has been already noted that a number of dwarf starburst galaxies contain highly luminous clusters much brighter that expected from the general size of their cluster population (NGC 1569, Anders et al. 2004b; NGC 1705, Billett et al. 2002; NGC 4449, Reines et al. 2008a; SBC 0335−052, Reines et al. 2008b). Larsen (2002) refers to NGC 1569 and 1705 as an example of possibly biased CLF towards high-mass clusters or in other words that CLF in those galaxies may be peculiar. If this is true, then BCGs are more similar in this respect to dwarf starburst galaxies than to very massive systems.

6.2 Cluster formation rate (CFR) versus SFR in Haro 11

The SFR in Haro 11 is very high. Hayes et al. (2007) found a SFR ∼19–25 $M_\odot$ yr^{-1}, using a wide range of estimators. Applying the relation in Rowan-Robinson et al. (1997) we calculated a total IR luminosity of $L_{FIR} = 4.43 \times 10^{44}$ erg s^{-1} from the IR luminosity at 60 μm (taken from NED). Using the total IR luminosity of Haro 11 we derived the present SFR from the Kennicutt's relation (Kennicutt 1998) of SFR = 21.1 $M_\odot$ yr^{-1}, in perfect agreement with the estimation made by Hayes et al. (2007). In this paper we used a mean value of the SFR = 22 ± 3 $M_\odot$ yr^{-1}.

Typically, a fraction of the star formation in the galaxy occurs in bound clusters, which will possibly survive and evolve. The remaining star formation occurs in low-mass clusters (analogous to the MW's open clusters), associations and more extended systems which would be destroyed during the first few Myr and dispersed into the field, as predicted by infant mortality. Bastian (2008) has defined the present cluster formation efficiency in a host galaxy as $\Gamma = CFR/SFR$, where CFR $= M_{tot}/\Delta t$ is the present CFR at which the galaxy produces a total cluster mass M_{tot} in a given age interval Δt. In a recent paper, Goddard, Bastian & Kennicutt (2010) have found a correlation between the value of Γ and the star formation density Σ_{SFR} of the hosting system, confirming that higher SFR leads to the formation of more bound clusters.

The cluster age distribution for Haro 11 shows that the present starburst has lasted for 40 Myr, with a peak of cluster formation only a few Myr ago. Under the condition that a full cluster population forms in 10 Myr, we tried to estimate how the rate of cluster formation has changed since the burst phase began. Taking into account the distance of the galaxy and possible blending at the faint end of the cluster mass function (CMF), we estimated the total mass in clusters more massive than 5×10^4 $M_\odot$ at each 10 Myr age bin, assuming that we detect all the clusters younger than 40 Myr with masses above this limit. In this way we have constructed the observed cluster formation history (CFH) in clusters more massive than 5×10^4 $M_\odot$ (Fig. 22). The CFH of massive clusters peaks
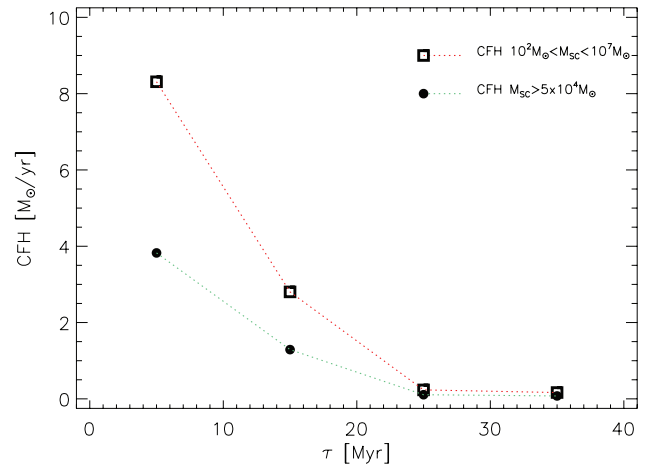
Figure 22. CFH of the present starburst in Haro 11. The filled black dots connected by the light grey (green online) dotted line shows the observed CFH estimated by the total mass in clusters more massive than 5×10^4 $M_\odot$. The open squares connected by the dotted grey line (red online) trace the extrapolated CFH for clusters with masses in the range 10^2 to 10^7 $M_\odot$, under the condition of an ICMF with index −2 and assuming that we know the total mass in clusters more massive than 5×10^4 $M_\odot$ in each age bin.

with the youngest cluster population, which has formed in the last 10 Myr at a rate of 3.8 $M_\odot$ yr^{-1}. This shows that at the present time, $\Gamma(M_{SC} > 5 \times 10^4 M_\odot) \sim 0.17$, or in other words, 17 per cent of the star formation is happening in massive clusters. The CFR declines towards lower rates at larger look-back times and reaches a value of 0.08 $M_\odot$ yr^{-1} when the cluster population formed around 40 Myr ago. This decline may also indicate lower SFRs at this epoch. However, the massive cluster formation in the galaxy during the whole period has been extremely efficient.

In order to constrain a total CFR, we estimated the missing fraction of mass in low-mass clusters ($10^2 < M_{SC} < 5 \times 10^4 M_\odot$), taking an initial CMF (ICMF) with slope −2 and assuming that the total cluster mass in the range 5×10^4–10^7 $M_\odot$ is known. The extracted total CFH is also shown in Fig. 22. The total CFR at ages below 10 Myr is 8.31 $M_\odot$ yr^{-1}, which means cluster formation efficiency $\Gamma \sim 0.38 \pm 0.6$ or ∼38 per cent. This fraction is extremely high compared to the value observed in cluster systems in other galaxies (see Table 4), and almost a factor of 10 higher than in the Small Magellanic Cloud (Γ = 2–4 per cent; Gieles & Bastian 2008) and the solar neighbourhood (∼5 per cent; Lada & Lada 2003). We reach the same result if we estimate the present CFR from the most massive cluster, M_{max}, in the age bin 1–10 Myr. In fact Gieles & Bastian (2008) showed that $M_{tot} \simeq 10M_{max}$, for a constant CFR and a power-law CIMF with index −2, and assuming that the maximum cluster mass formed by the galaxy, M_{up}, is bigger than the M_{max} observed in the system. If we assume that the CFR is constant over the last 10 Myr and that the most massive cluster formed[10] is knot B with a mass of 8.35×10^6 $M_\odot$, the present CFR is 8.35 $M_\odot$ yr^{-1}, very similar to the value estimated above.

If blending affects our cluster mass estimates then we may be overestimating the CFR. Applying the relation found by Goddard et al. (2010) between Γ (per cent) and Σ_{SFR}, we can estimate the expected value of Γ for the SFR observed in Haro 11. The starburst

---

[10] The very massive region C is excluded due to the uncertainties in its SED fit.

Table 4. The cluster population of Haro 11 compared to the galaxy sample of Goddard et al. (2010). We show the SFR, Γ (per cent), and total mass in clusters younger than 10 Myr and more massive than $10^3 \, M_\odot$ (NGC 1569, M83, NGC 6946) or $5 \times 10^4 \, M_\odot$ (NGC 3256 and Haro 11), M_{YSC}, the total hosting galaxy mass, M_{gal}, and the fraction of the total cluster mass with respect to the galactic mass, $f = M_{YSC}/M_{gal}$. The data of the galaxies NGC 1569, M83, NGC 6946 and 3256 are from Goddard et al. (2010) unless otherwise specified.

Galaxy	SFR ($M_\odot$ yr^{-1})	Γ (per cent)	M_{YSC} ($M_\odot$)	M_{gal} ($M_\odot$)	f
NGC 1569	0.3626	13.9 ± 0.8	3.52×10^5	4.6×10^{8a}	0.0008
M83	0.3867	$26.7^{5.3}_{4.0}$	7.24×10^5	6.1×10^{10b}	1.5×10^{-5}
NGC 6946	0.1725	$12.5^{1.8}_{2.5}$	1.284×10^5	5×10^{10c}	2.6×10^{-6}
NGC 3256	46.17	$22.9^{7.3}_{9.8}$	1.66×10^7	$\sim 5 \times 10^{10d}$	0.0003
Haro 11	22 ± 3	38 ± 6	3.82×10^7	$\sim 1 \times 10^{10}$	0.004

[a]Israel (1988); [b]Lundgren et al. (2004); [c]Walsh et al. (2002); [d]Feast & Robertson (1978).
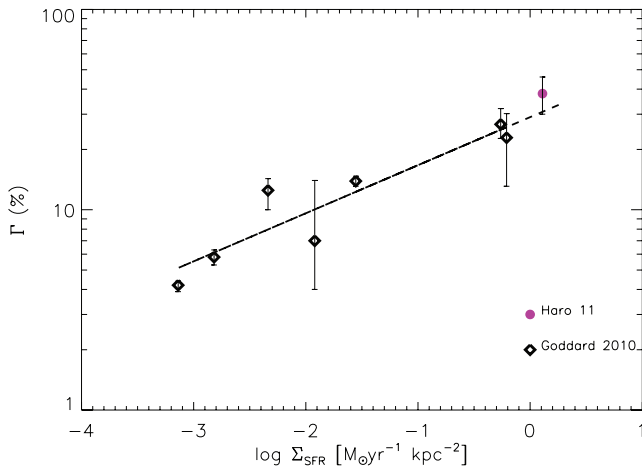
Figure 23. Cluster formation efficiency, Γ, as a function of the galactic SFR density, Σ_{SFR}. The black diamonds are the galaxy sample of Goddard et al. (2010) which were used to obtain the best-fitting power-low relation shown by the dashed line (Goddard et al. 2010, their equation 3). At the right-hand end we show the position of Haro 11 (filled dots) which fits the relation nicely despite its extreme Γ and SFR values.

6.3 Discussion

In a recent work, Melena et al. (2009) studied the properties of clumpy star-forming regions associated with bound clusters in nearby dwarf starburst galaxies. They found that, independently of their environmental conditions, the formation of those clumps is given by random sampling of a mass function of the form $dN/dM \propto M^{-2}$. We can think the mass function as a statistical relation which is stochastically realized by star formation in clusters. The galactic environment limits the range of the stochastic action. For example, the galactic environmental conditions can limit the maximum possible mass at which a cluster can be formed (Gieles et al. 2006a). The galactic environment may also lead to a characteristic mass, M_c, above which a CIMF shaped like a Schechter function declines exponentially (Gieles 2009; Larsen 2009a). In particular, Larsen (2009a) noted that extreme star-forming environments show no characteristic truncation at $10^5 < M_c < 10^6$ because such galaxies are actually able to form very massive clusters ($M > 10^6$). Larsen (2009a) presented two hypotheses regarding the physical mechanism responsible for the formation of massive clusters. In the first, such clusters are formed by super-GMCs, with masses of at least 10^7–$10^8 \, M_\odot$. The second requires a higher SFE during the collapse of the GMC, which in turn implies compression of the gas to higher densities. In the MW it has been observed that GMCs have low densities and form clusters with low SFE (Lada & Lada 2003) producing low-mass clusters. In quiescent massive regular spirals like the MW the shear due to the spiral patterns would then favour the fragmentation of GMCs, preventing very massive clusters from forming. On the other hand, as pointed out by Billett et al. (2002), in dwarf starburst systems the gravitational instabilities acting on the GMCs are instead much stronger than the shear from the irregular intergalactic medium, allowing the observed massive clusters to form.

In Haro 11 we have found many massive clusters, over 35 per cent of which have masses above $10^5 \, M_\odot$. In the previous section we showed that the efficiency with which the galaxy has formed clusters, in particular massive clusters, is higher than in merging systems like NGC 3256. Haro 11 has an irregular morphology and is less massive than normal spiral galaxies. It seems likely that a previous merger with a gas-rich system has favoured the inflow and compression of gas, triggering the formation of the massive clusters. In this way, the galaxy, despite its peculiarities, easily fits into the wider picture of a sequence in star formation intensity stretching from quiescent to very active modes according to Goddard's relation. The age distribution of the clusters confirms the present estimated starburst age of ~ 35 Myr found by Östlin et al. (2001).

in this galaxy covers an area of ~ 2.34 kpc^2 so that the $\Sigma_{SFR} = 1.28 \, M_\odot$ yr^{-1} kpc^{-2}. From equation (3) in Goddard et al. (2010) we find that $\Gamma = 31.0 \pm 5$ per cent which is in quite good agreement with the previously found value. In Fig. 23 we show the relation presented by Goddard et al. (2010) and the galaxy sample they used to derive it, with the addition of the position of Haro 11. We observed that in spite of the extreme cluster formation environment in Haro 11, the correlation found by Goddard et al. (2010) between Γ and density of SFR is still valid, supporting the theory of a close connection between the global properties of the host galaxy and its SC population.

In Table 4 we summarize the properties of the Goddard et al. sample together with Haro 11. For some of the objects the authors gave the total mass contained in clusters younger than 10 Myr. We used these values to estimate at which fraction of the total mass of the system they do correspond, as indicated in the last column of Table 4. For Haro 11 we used only the total observed mass in clusters more massive than $5 \times 10^4 \, M_\odot$. The comparison between the values for different galaxies nevertheless gives an idea of the strength of the cluster formation process in Haro 11.

The starburst has propagated rapidly through the entire galaxy as showed in Fig. 20, consuming the available fuel and is possibly now settling into a period of more modest activity, as attested by the low H I mass content in the galaxy Bergvall et al. 2000. From the available H I mass, the remaining lifetime of the present burst phase is ∼5 Myr.

A final important issue is raised by the similarity between Haro 11 and LBGs observed at high redshift (Overzier et al. 2008). Nearby Lyman break analogues (LBAs) are attractive objects for studying star formation modes and morphology in detail which is impossible at high redshift. Overzier et al. (2009) have, for example, shown that star formation in LBAs is both very active and concentrated in clumpy regions which may be composed of supermassive SCs. In Haro 11, we found a CFR of 38 per cent, somewhat higher than locally observed. This result suggests that the CFRs in LBGs could be almost a factor of 10 higher than that in the Local Group, implying that at high-redshift galaxies formed more numerous and more massive clusters than we observe in the local Universe. However, investigation of other systems similar to Haro 11 is needed before we can draw firm conclusions.

7 CONCLUSIONS

Thanks to the deep *HST* data stretching from UV to IR wavebands, we have carried out a photometric study of the clusters in the starburst regions of Haro 11. We have constrained the physical properties of 185 clusters through the analysis of their integrated SEDs. We summarize the main results here.

(i) More than 60 per cent of the SCs in Haro 11 are younger than 10-Myr old. The present starburst phase started less than 40 Myr ago with a peak as recently as 3.5 Myr. Only 16 clusters have estimated ages greater than 40 Myr and, of these, half are older than >100 Myr. Haro 11 therefore provides a unique opportunity to investigate the cluster formation and evolution in a starburst system in its earliest phases. For ages between 1 and 3.5 Myr the extinction range is quite wide, consistent with a complex cluster formation process and the gradual dissolution of the parent clouds.

(ii) The clusters are quite massive, with masses between 10^3 and $10^6 \, M_\odot$. There are around 60 estimated SSCs, seven of them with masses larger than $10^6 \, M_\odot$, and two very massive knots (B and C) with estimated masses $\geq 10^7 \, M_\odot$ which we could not resolve into smaller clusters. Very young clusters (1–3 Myr) with masses around 10^3–$10^4 \, M_\odot$ are absent from our data even though our detection limits should have allowed their detection. These missing clusters could still be embedded in their parental clouds, invisible in optical wavebands, or blended with other clusters in the most crowded regions.

(iii) We have discovered that a fraction of the clusters exhibits a flux excess compared to plausible SED models at wavelengths >8000 Å. We have noted that fitting those cluster SEDs affected by the red excess with normal SSP models leads to overestimation of the cluster ages and masses. In several cases, we have obtained acceptable fits only at bands blueward of *I*, highlighting the potential impact of the phenomenon on estimations of the cluster properties. Of the clusters affected by the red excess, none is older than 40 Myr.

(iv) We have discussed possible causes for the red excess. If the age of the cluster is the key property, then the red excess in clusters younger than 5 Myr could be due to the simultaneous presence of very young UV-bright massive stars and the dust left from the GMCs. The ERE mechanism could then originate the excess at *I* waveband while hot dust emission produces a 'rise' at IR wave-

lengths, depending on the size and temperature of the dust grains. Another possible mechanism at such young stages could be the presence in the cluster of two stellar components, one of which has shed its dust envelope, contributing mainly in the UV–optical wavelengths, while the other component is still deeply embedded in its star-forming cloud and highly extinguished. Pre-main-sequence objects and YSOs still surrounded by circumstellar discs can produce this IR-bright component. Further modelling will be required in order to estimate how massive the second stellar component needs to be in order to produce such large displacements in the *H* and K_s bands. The presence of such embedded stellar populations emitting only in the IR would also imply that the mass of these clusters will be underestimated. At ages >5 Myr we expect that the embedded phase is over; we have suggested two further mechanisms to explain the NIR excess for ages older than this. First, evolved clusters may be observed in the line of sight towards younger, embedded ones. In such cases, the cluster behind would only be visible at IR bands, while the age and mass estimated from UV and optical bands correspond to the cluster in front. Secondly, RSGs, which dominate the light at red and near-IR wavelengths, could 'redden' the observed colours of the clusters at ages as early as 6 Myr.

(v) For the first time, after an early attempt by Östlin et al. (2003), we have analysed the CLF in a BCG. Haro 11's CLF is shallower than that observed in other galaxies. Contamination by blending could have this effect on the CLF, but we did not find any evidence of overestimation of the CFR using the more massive SCs. Obviously, at the distance of the galaxy and with the present available data, we cannot avoid crowding and projection contaminations.

(vi) More than 30 per cent of the star formation in Haro 11 has happened in bound clusters which can survive and evolve along with the galaxy. This fraction is higher than that observed in the MW and other merging galaxies like NGC 3256, leading to the conclusion that the environmental conditions in this BCG have favoured the formation of massive SSCs. Due to the similarities between Haro 11 and the high-redshift LBGs, we suggest that CFRs at higher redshift may also be enhanced.

REFERENCES

Adamo A., Östlin G., Zackrisson E., Hayes M., 2009, preprint (arXiv:0907.3059)

Anders P., Fritze-Alvensleben U., 2003, A&A, 401, 1063

Anders P., Bissantz N., Fritze-v. Alvensleben U., de Grijs R., 2004a, MNRAS, 347, 196

Anders P., de Grijs R., Fritze-v. Alvensleben U., Bissantz N., 2004b, MNRAS, 347, 17

Annibali F., Tosi M., Monelli M., Sirianni M., Montegriffo P., Aloisi A., Greggio L., 2009, AJ, 138, 169

Bastian N., 2008, MNRAS, 390, 759

Bastian N., Gieles M., Lamers H. J. G. L. M., Scheepmaker R. A., de Grijs R., 2005, A&A, 431, 905

Bastian N., Covey K. R., Meyer M. R., 2010, preprint (arXiv:1001.2965)
Bergvall N., Östlin G., 2002, A&A, 390, 891
Bergvall N., Masegosa J., Östlin G., Cernicharo J., 2000, A&A, 359, 41
Bertin E., Arnouts S., 1996, A&AS, 117, 393
Bik A., Lamers H. J. G. L. M., Bastian N., Panagia N., Romaniello M., 2003, A&A, 397, 473
Billett O. H., Hunter D. A., Elmegreen B. G., 2002, AJ, 123, 1454
Calzetti D., Armus L., Bohlin R. C., Kinney A. L., Koornneef J., Storchi-Bergmann T., 2000, ApJ, 533, 682
Cantiello M., Brocato E., Blakeslee J. P., 2009, A&A, 503, 87
Cerviño M., Luridiana V., 2004, A&A, 413, 145
Clegg R. E. S., Middlemass D., 1987, MNRAS, 228, 759
Cresci G., Vanzi L., Sauvage M., 2005, A&A, 433, 447
de Grijs R., Fritze-v. Alvensleben U., Anders P., Gallagher J. S., Bastian N., Taylor V. A., Windhorst R. A., 2003a, MNRAS, 342, 259
de Grijs R., Anders P., Bastian N., Lynds R., Lamers H. J. G. L. M., O'Neil E. J., 2003b, MNRAS, 343, 1285
Dolphin A. E., 2009, PASP, 121, 655
Elmegreen B. G., 2010, IAUS, 266, 3
Feast M. W., Robertson B. S. C., 1978, MNRAS, 185, 31
Ferland G. J., Korista K. T., Verner D. A., Ferguson J. W., Kingdon J. B., Verner E. M., 1998, PASP, 110, 761
Fernández-Ontiveros J. A., Prieto M. A., Acosta-Pulido J. A., 2009, MNRAS, 392, L16
Fitzpatrick E. L., 1986, AJ, 92, 1068
Fouesneau M., Lançon A., 2009, preprint (arXiv:0908.2742)
Fruchter A. S., Hook R. N., 2002, PASP, 114, 144
Galametz M. et al., 2009, A&A, 508, 645
Gieles M., 2009, MNRAS, 394, 2113
Gieles M., Bastian N., 2008, A&A, 482, 165
Gieles M., Larsen S. S., Bastian N., Stein I. T., 2006a, A&A, 450, 129
Gieles M., Larsen S. S., Scheepmaker R. A., Bastian N., Haas M. R., Lamers H. J. G. L. M., 2006b, A&A, 446, L9
Goddard Q. E., Bastian N., Kennicutt R. C., 2010, MNRAS, doi: 10.1111/j.1365-2966.2010.16511.x
Hayes M., Östlin G., Atek H., Kunth D., Mas-Hesse J. M., Leitherer C., Jimnez-Bailn E., Adamo A., 2007, MNRAS, 382, 1465
Hunter D. A., Elmegreen B. G., Dupuy T. J., Mortonson M., 2003, AJ, 126, 1836
Israel F. P., 1988, A&A, 194, 24
Kennicutt R. C. Jr, 1998, ARA&A, 36, 189
Koekemoer A. M., Fruchter A. S., Hook R. N., Hack W., 2002, in Arribas S., Koekemoer A., Whitmore B., eds, The 2002 *HST* Calibration Workshop: Hubble After the Installation of the ACS and the NICMOS Cooling System. p. 337
Konstantopoulos I. S., Bastian N., Smith L. J., Westmoquette M. S., Trancho G., Gallagher J. S., 2009, ApJ, 701, 1015
Kroupa P., 2001, MNRAS, 322, 231
Krüger H., Fritze-v. Alvensleben U., Loose H.-H., 1995, A&A, 303, 41
Kunth D., Östlin G., 2000, A&AR, 10, 1
Kunth D., Maurogordato S., Vigroux L., 1988, A&A, 204, 10
Kunth D., Leitherer C., Mas-Hesse J. M., Östlin G., Petrosian A., 2003, ApJ, 597, 263
Lada C. J., 2010, R. Soc. London Philos. Trans. Series A, 368, 713
Lada C. J., Lada E. A., 2003, ARA&A, 41, 57
Lançon A., Fouesneau M., 2009, preprint (arXiv:0903.4557)
Lançon A., Mouhcine M., 2002, A&A, 393, 167
Larsen S. S., 1999, A&AS, 139, 393
Larsen S. S., 2002, AJ, 124, 1393
Larsen S. S., 2009a, A&A, 494, 539
Larsen S. S., 2009b, preprint (arXiv:0911.0796)
Lejeune T., Cuisinier F., Buser R., 1998, A&AS, 130, 65
Lundgren A. A., Olofsson H., Wiklind T., Rydbeck G., 2004, A&A, 422, 865
Maíz Apellániz J., 2009, ApJ, 699, 1938
Marigo P., Girardi L., Bressan A., Groenewegen M. A. T., Silva L., Granato G. L., 2008, A&A, 482, 883 (M08)

Melena N. W., Elmegreen B. G., Hunter D. A., Zernow L., 2009, AJ, 138, 1203
Melo V. P., Muñoz-Tuñón C., Maíz-Apellániz J., Tenorio-Tagle G., 2005, ApJ, 619, 270
Mengel S., Lehnert M. D., Thatte N., Genzel R., 2005, A&A, 443, 41
Micheva G., Zackrisson E., Östlin G., Bergvall N., Pursimo T., 2010, MNRAS, in press (arXiv:1002.3826)
Misselt K. A., Clayton G. C., Gordon K. D., 1999, ApJ, 515, 128
Östlin G., Amram P., Bergvall N., Masegosa J., Boulesteix J., Márquez I., 2001, A&A, 374, 800
Östlin G., Zackrisson E., Bergvall N., Rönnback J., 2003, A&A, 408, 887
Östlin G., Hayes M., Kunth D., Mas-Hesse J. M., Leitherer C., Petrosian A., Atek H., 2009, AJ, 138, 923
Overzier R. A. et al., 2008, ApJ, 677, 37
Overzier R. A. et al., 2009, ApJ, 706, 203
Press W. H., Teukolsky S. A., Vetterling W. T., Flannery B. P., 1992, Numerical Recipes in FORTRAN. The Art of Scientific Computing, 2nd edn. Cambridge Univ. Press, Cambridge
Reines A. E., Johnson K. E., Goss W. M., 2008a, AJ, 135, 2222
Reines A. E., Johnson K. E., Hunt L. K., 2008b, AJ, 136, 1415
Reines A. E., Nidever D. L., Whelan D. G., Johnson K. E., 2010, ApJ, 708, 26
Rowan-Robinson M. et al., 1997, MNRAS, 289, 490
Smith B. J., Hancock M., 2009, AJ, 138, 130
Väisänen P. et al., 2008, MNRAS, 384, 886
Walsh W., Beck R., Thuma G., Weiss A., Wielebinski R., Dumke M., 2002, A&A, 388, 7
Westmoquette M. S., Smith L. J., Gallagher J. S. III, O'Connell R. W., Rosario D. J., de Grijs R., 2007, ApJ, 671, 358
Whitmore B. C., Zhang Q., 2002, AJ, 124, 1418
Whitmore B. C., Zhang Q., Leitherer C., Fall S. M., Schweizer F., Miller B. W., 1999, AJ, 118, 1551
Wilson C. D., Harris W. E., Longden R., Scoville N. Z., 2006, ApJ, 641, 763
Witt A. N., Vijh U. P., 2004, in Witt A. N., Clayton G. C., Drain B. T., eds, ASP Conf. Ser. Vol. 309, Astrophysics of Dust. Astron. Soc. Pac., San Francisco, p. 115
Zackrisson E., Bergvall N., Olofsson K., Siebert A., 2001, A&A, 375, 814 (Z01)
Zackrisson E., Bergvall N., Leitet E., 2008, ApJ, 676, L9
Zhang Q., Fall S. M., 1999, ApJ, 527, L81

APPENDIX A: CHECK ON THE CALIBRATION OF THE *F160W* FRAME

We performed two different tests on the *HST* IR frame in order to verify the goodness of the calibration. First, we compared photometry output of few bright sources between the final reduced frame and one single raw frame. At the same aperture radius, sources on the raw frame showed to be ∼0.15 mag brighter than the final science frame. However, this scatter can be explained by sky background and bias-effect corrections performed on the final frame. In the second test, we used an available *HST* archive NIC2/*F160W* exposure of the MRK 930 target. Because of the analogy between the NIC3 data set of Haro 11 and MRK 930 we decided to compare the photometry outputs of MRK 930 NIC2 and NIC3 *F160W* frames. The NIC2 frames were reduced with MULTIDRIZZLE. For small aperture radii, the photometry of sources in the NIC2 frame were brighter than that in the NIC3 ones with a similar constant scatter. At larger radii, the scatter became rapidly negligible. As expected this behaviour is due to the better pixel resolution scale and PSF sampling of the NIC2 camera. However, because the photometry converged at the same values this shows the correctness of the calibration, showing at the same time the importance of an accurate aperture correction to infinity.

APPENDIX B:

Table B1. Photometric properties of the four clusters showed in Fig. 4. Magnitudes are in Vega system throughput.

ID	*F606W*	*F814W*	*F140LP*	*F220W*	*F330W*	*F435W*	*F550M*	*F160W*	$K_{\rm s}$
6	22.97 ± 0.1	22.67 ± 0.07	20.75 ± 0.06	21.25 ± 0.07	22.10 ± 0.08	23.12 ± 0.05	23.21 ± 0.06	21.24 ± 0.42	20.18 ± 0.66
43	21.49 ± 0.11	20.81 ± 0.05	21.70 ± 0.11	21.73 ± 0.13	21.59 ± 0.09	22.54 ± 0.08	22.33 ± 0.07	19.07 ± 0.4	17.71 ± 0.64
87	22.32 ± 0.19	22.16 ± 0.17	19.84 ± 0.12	20.51 ± 0.14	–	22.60 ± 0.15	22.42 ± 0.13	–	19.21 ± 0.66
113	22.49 ± 0.1	22.09 ± 0.05	–	–	–	23.29 ± 0.06	22.85 ± 0.06	21.11 ± 0.42	20.12 ± 0.66

This paper has been typeset from a TEX/LATEX file prepared by the author.